Colloquium : Multiconfigurational time-dependent Hartree approaches for indistinguishable particles

Axel U. J. Lode, Camille Lévêque, Lars Bojer Madsen, Alexej I Streltsov, Ofir E Alon

Colloquium: Multiconfigurational time-dependent Hartree approaches for indistinguishable particles

Axel U. J. Lode*

Institute of Physics, Albert-Ludwig University of Freiburg, Hermann-Herder-Strasse 3, 79104 Freiburg, Germany, Vienna Center for Quantum Science and Technology, Atominstitut, TU Wien, Stadionallee 2, 1020 Vienna, Austria, and Wolfgang Pauli Institute c/o Faculty of Mathematics, University of Vienna, Oskar-Morgenstern Platz 1, 1090 Vienna, Austria

Camille Lévêque

Vienna Center for Quantum Science and Technology, Atominstitut, TU Wien, Stadionallee 2, 1020 Vienna, Austria and Wolfgang Pauli Institute c/o Faculty of Mathematics, University of Vienna, Oskar-Morgenstern Platz 1, 1090 Vienna, Austria

Lars Bojer Madsen

Department of Physics and Astronomy, Aarhus University, 8000 Aarhus C, Denmark

Alexej I. Streltsov

Theoretische Chemie, Physikalisch-Chemisches Institut, Universität Heidelberg, Im Neuenheimer Feld 229, D-69120 Heidelberg, Germany

Ofir E. Alon

Department of Mathematics, University of Haifa, Haifa 3498838, Israel and Haifa Research Center for Theoretical Physics and Astrophysics, University of Haifa, Haifa 3498838, Israel

(published 27 February 2020)

In this Colloquium, the wave-function-based multiconfigurational time-dependent Hartree approaches to the dynamics of indistinguishable particles (MCTDH-F for fermions and MCTDH-B for bosons) are reviewed. MCTDH-B and MCTDH-F or, together, MCTDH-X are methods for describing correlated quantum systems of identical particles by solving the time-dependent Schrödinger equation from first principles. MCTDH-X is used to accurately model the dynamics of real-world quantum many-body systems in atomic, molecular, and optical physics. The key feature of these approaches is the time dependence and optimization of the single-particle states employed for the construction of a many-body basis set, which yields nonlinear working equations. The historical developments that have led to the formulation of the MCTDH-X method and motivate the necessity for wave-function-based approaches are briefly described. The derivation of the unified MCTDH-F and MCTDH-B equations of motion for complete and also specific restricted configuration spaces are sketched. The strengths and limitations of the MCTDH-X approach are assessed via benchmarks against an exactly solvable model and via convergence checks. Applications to some instructive and experimentally realized quantum many-body systems are highlighted: the dynamics of atoms in Bose-Einstein condensates in magneto-optical and optical traps and of electrons in atoms and molecules. The current development and frontiers in the field of MCTDH-X are discussed: theories and numerical methods for indistinguishable particles, for mixtures of multiple species of indistinguishable particles, the inclusion of nuclear motion for the nonadiabatic dynamics of atomic and molecular systems, as well as the multilayer and second-quantized-representation approaches, and the orbital-adaptive time-dependent coupled-cluster theory.

DOI: 10.1103/RevModPhys.92.011001

*auj.lode@gmail.com

CONTENTS

I. INTRODUCTION

This Colloquium introduces and discusses the development and capabilities of the multiconfigurational time-dependent Hartree (MCTDH) approaches (Meyer, Manthe, and Cederbaum, 1990; Manthe, Meyer, and Cederbaum, 1992; Beck *et al.*, 2000) for solving the time-dependent many-body Schrödinger equation of indistinguishable particles with a focus on MCTDH-F for fermions (Zanghellini *et al.*, 2003; Kato and Kono, 2004; Caillat *et al.*, 2005) and MCTDH-B for bosons (Streltsov, Alon, and Cederbaum, 2007; Alon, Streltsov, and Cederbaum, 2008) or, together, MCTDH-X (Alon, Streltsov, and Cederbaum, 2007c).

The time-dependent many-body Schrödinger equation for interacting, indistinguishable particles is a cornerstone of many areas of physics. Exactly solvable models are very scarce for both the time-dependent (Lode, Sakmann *et al.*, 2012; Lode, 2015; Fasshauer and Lode, 2016) and the time-independent Schrödinger equations (Girardeau, 1960; Lieb, 1963; Lieb and Liniger, 1963; Luttinger, 1963; Mcguire, 1964; Mattis and Lieb, 1965; Calogero, 1969; Sutherland, 1971; Haldane, 1981; Dukelsky and Schuck, 2001; Yukalov and Girardeau, 2005) and could so far not be generalized to real-world problems. A numerical approach to tackle the Schrödinger equation is therefore widely needed. The direct numerical solution of the Schrödinger equation, however, quickly becomes impracticable. The Hilbert space in which the generally high-dimensional solution of the Schrödinger equation lives grows exponentially with the number of particles considered. As a consequence of this so-called curse of dimensionality, solutions even for very few particles are out of reach with the direct approach, especially in the case of inhomogeneous systems.

To numerically solve the Schrödinger equation nevertheless, one has to overcome the curse of dimensionality with the help of a clever approximate representation of the solution. Here "clever" means that the problem has to be represented accurately enough to cover the physical properties of the many-body state while, at the same time, the chosen representation has to be sufficiently compact to be manageable computationally. Since the time-dependent many-body Schrödinger equation is so fundamental, there exist many approximations to its solution. Each new methodology is a step in the quest for an ever more accurate description.

Examples for obtaining a numerically tractable representation for the state include the multiorbital mean-field (Gross, 1961; Pitaevskii, 1961; McLachlan and Ball, 1964; Alon, Streltsov, and Cederbaum, 2007b) and the configuration interaction (Szabo and Ostlund, 1996; Sherrill and Schaefer, 1999; Rook, 2006; Bassaganya-Riera and Hontecillas, 2015) approaches. Mean-field approaches, however, drop all of the correlations from the description of the many-body state by representing the wave function as a single symmetrized or antisymmetrized product of one or more time-dependent single-particle states. Configuration interaction or exact diagonalization includes correlations, but is restricted to situations where the initially chosen, time-independent basis remains suitable for all times (Lode, Sakmann *et al.*, 2012; Lode, 2015).

For Hubbard models there exist, for instance, the time-dependent density matrix renormalization group [see the review by Schollwöck (2005) and references therein], matrix product states [see the review by Schollwöck (2011) and references therein], and time-evolved block decimation methods (Zwolak and Vidal, 2004). These latter methods describe correlated many-body dynamics for Hubbard lattices, but are not directly applicable in other cases.

The MCTDH-X (Zanghellini *et al.*, 2003; Kato and Kono, 2004; Caillat *et al.*, 2005; Alon, Streltsov, and Cederbaum, 2007c, 2008; Streltsov, Alon, and Cederbaum, 2007) methods can describe correlations in the dynamics of many-body systems that are not necessarily described by model Hamiltonians. Two basic ingredients were needed to obtain MCTDH-X: (i) a unification of the *time-independent* basis of configuration interaction with the *time-adaptive Ansatz* of the (multiorbital) mean field [also referred to as time-dependent Hartree-Fock (TDHF) or self-consistent field methods] for indistinguishable particles and (ii) an appropriate time-dependent variational principle (Dirac, 1927; Frenkel, 1934; McLachlan, 1964; Kramer and Saraceno, 2007).

MCTDH-X is a general method for the solution of the time-dependent many-body Schrödinger equation (TDSE) for interacting indistinguishable particles that yields a well-controlled error (Lode, Sakmann *et al.*, 2012; Lode, 2015; Fasshauer and Lode, 2016) and constitutes the main subject of this Colloquium. To introduce and motivate MCTDH-X, we give an account of the theoretical development that led to its formulation. We illustrate the insight into many-body physics

gained thus far from applications of MCTDH-X in the areas of atomic, molecular, and optical physics with applications to real-world, experimentally realized examples of the dynamics of atoms in trapped Bose-Einstein condensates (BECs) and electrons in atoms and molecules. Finally, theoretical and numerical developments, in particular, the species- or coordinate-multilayer MCTDH-X (Cao *et al.*, 2013, 2017; Krönke *et al.*, 2013) and the multilayer (ML) MCTDH in second-quantized representation (SQR) (Wang and Thoss, 2009), as well as prospects and possible future avenues of the MCTDH-X approaches are outlined. We note that the ML-MCTDH-SQR theory uses a multiconfigurational *Ansatz* directly formulated in Fock space and is thus distinct from MCTDH-X; see details later. For reference and orientation, we collected some important acronyms in the List of Symbols and Abbreviations at the end of the main text.

In Sec. II, we provide a unified formulation of the equations of motion (EOMs) of MCTDH-X for complete as well as restricted configuration spaces, i.e., for situations where all or only part of the possible Slater determinants or permanents are included in the wave function, respectively. For simplicity and instructiveness, we restrict our discussion to the so-called restricted active space approach. In Sec. II.C, we conclude our exhibition of the MCTDH-X approaches with benchmarks using an exactly solvable model problem, the harmonic interaction model, which show that the method is in principle exact (Lode, Sakmann *et al.*, 2012; Lode, 2015; Fasshauer and Lode, 2016).

In Sec. III, we focus on MCTDH-B applications to the physics of quantum correlations and fluctuations and the variance of operators in BECs. We summarize an illustrative application of MCTDH-B to the dynamics of a BEC subject to time-dependent interparticle interactions where computations were directly compared to experiment (Nguyen *et al.*, 2019). Moreover, we highlight some insight into the intriguing physics of the variances of observables in the so-called infinite-particle-number limit (Klaiman and Alon, 2015; Alon and Cederbaum, 2018) that were obtained with the help of MCTDH-B.

In Sec. IV, we discuss some insights that MCTDH-F has delivered for the correlated dynamics of electrons in atoms and molecules. We give an account of work using MCTDH-F with a focus on studies of photoionization cross sections and time delays that were experimentally verified (Haxton, Lawler, and McCurdy, 2012; Omiste and Madsen, 2018).

In Sec. V we provide an overview of current theoretical progress with MCTDH-X and related multiconfigurational methods as well as possible future avenues of method development. We discuss the key ideas of the ML approach (Wang and Thoss, 2003; Manthe, 2008) and its application to multiconfigurational methods to obtain the dynamics of indistinguishable particles, i.e., the ML-MCTDH in (optimized) second-quantized representation, ML-MCTDH-(o)SQR (Wang and Thoss, 2009; Manthe and Weike, 2017; Weike and Manthe, 2020) and the ML-MCTDH-X (Cao *et al.*, 2013, 2017; Krönke *et al.*, 2013). Moreover, we discuss generalizations of MCTDH-B (Grond *et al.*, 2013; Alon, Streltsov, and Cederbaum, 2014) and MCTDH-F (Sato and Ishikawa, 2015; Sawada, Sato, and Ishikawa, 2016; Lötstedt, Kato, and Yamanouchi, 2019b) as well as orbital-adaptive time-dependent coupled-cluster theories (Kvaal, 2012, 2013; Sato *et al.*, 2018a, 2018b; Pedersen and Kvaal, 2019).

This Colloquium thus gives an overview of the activities in the community that develops and applies multiconfigurational methods for indistinguishable particles with a focus on MCTDH-X. Achievements made using the method on ultracold atoms in BECs and the correlated dynamics of electrons in atoms and molecules are illustrated and the state-of-the-art developments on the theory in the field of multiconfigurational methods for the dynamics of indistinguishable particles [MCTDH-X, ML-MCTDH-X, ML-MCTDH-(o)SQR] are introduced.

II. MCTDH-X THEORY

To obtain the MCTDH-X equations, one applies a variational principle to the TDSE with a parametrized *Ansatz*. As Kramer and Saraceno (2007) aptly assessed:

> "As is well-known, a variational principle is a blind and dumb procedure that always provides an answer, but its accuracy depends crucially on the choice of the trial function."

Different types of *Ansätze* thus lead to approximations with different qualitative behavior. Generally, the MCTDH-X type of *Ansatz* is a time-dependent linear combination of a set of fully symmetrized or antisymmetrized products of time-dependent single-particle states or orbitals, the so-called configurations. We ask the following: Why is the MCTDH-X *Ansatz* for the wave function a good *Ansatz*? One, the time-dependent configurations in the MCTDH-X *Ansatz* are an in-principle complete basis of N-particle Hilbert space and, two, they are constructed such that they are strictly orthonormalized at any time. These two properties, in combination with the time-dependent variational principle, allow one to infer the convergence of the method: if a sufficiently large set of configurations has been included in a computation, i.e., the result remains identical when more configurations are included, one can conclude that the employed *Ansatz* spans a sufficiently large portion of N-particle Hilbert space.

Here we discuss the archetypical MCTDH-X theory with an *Ansatz* (Caillat *et al.*, 2005; Alon, Streltsov, and Cederbaum, 2007c, 2008) including all possible configurations of N particles in M orbitals. We also cover the formulation of MCTDH-X with an *Ansatz* obtained with a further truncation of Hilbert space via the restricted active space (RAS) approach (Olsen *et al.*, 1988) as introduced by Miyagi and Madsen (2013) and Lévêque and Madsen (2017). We note that the RAS approach originates from quantum chemistry, but, although physical insight into the emergent quantum dynamics may help to choose a sensible RAS scheme, it may not be the best choice for the emergent dynamics of many-body systems. The EOMs of MCTDH-X for completely general configuration spaces, of which the RAS is a special case, have been mentioned for a single kind of indistinguishable particles by Haxton and McCurdy (2015) and even for multiple species of indistinguishable particles by Anzaki, Sato, and Ishikawa (2017). We chose to present the specialized RAS truncation scheme for MCTDH-X in this Colloquium, because

applications of it exist for both fermions and bosons. Moreover, as a truncation scheme we found the construction of the RAS instructive, illustrative, and simple, while the obtained EOMs hint at some of the changes triggered by the truncation of the Hilbert space in comparison to the standard MCTDH-X with a complete configuration space.

Moreover, as common for ultracold atoms and electron and nuclear dynamics, we focus on Hamiltonians of the form

$$\hat{H} = \sum_{i=1}^{N} \hat{h}(\mathbf{r}_i; t) + \sum_{i<j}^{N} W(\mathbf{r}_i, \mathbf{r}_j; t). \tag{1}$$

Here the position and spin of the kth particle are denoted by $\mathbf{r}_k$, $\hat{h}(\mathbf{r}; t)$ is a general, possibly time-dependent, single-particle operator and $\hat{W}(\mathbf{r}, \mathbf{r}'; t)$ is a general, possibly time-dependent, two-particle operator.

A. Unified equations of motion

We now discuss the EOMs of MCTDH-X and their derivation for the case where all possible configurations of N particles in M *time-dependent* orbitals are included in the *Ansatz*,

$$|\Psi^{\mathrm{FCI}}\rangle = \sum_{\vec{n}} C_{\vec{n}}(t)|\vec{n}; t\rangle; \;\; \vec{n} = (n_1, \ldots, n_M)^T,$$
$$|\vec{n}; t\rangle = \mathcal{N} \prod_{i=1}^{M} [\hat{b}_i^\dagger(t)]^{n_i}|\mathrm{vac}\rangle. \tag{2}$$

See Fig. 1 for an illustration of the MCTDH-X configuration space and the ansatz in Eq. (2). Here the normalization $\mathcal{N}$ is

$$\frac{1}{\sqrt{\prod_{i=1}^{M} n_i!}}$$

for bosons and $1/\sqrt{(N!)}$ fermions. The number of particles N is considered constant, $N = \sum_i n_i$, and $\hat{b}_j^\dagger(t)$ creates a particle in the single-particle state $\Phi_j(\mathbf{r}; t)$,

$$\Phi_j(\mathbf{r}, t) = \langle \mathbf{r}|\hat{b}_j^\dagger(t)|\mathrm{vac}\rangle. \tag{3}$$

Here, and in the following, we use the symbol $\mathbf{r}$ to summarize the degrees of freedom (spin and space) of the orbitals. The coefficients

$$C_{\vec{n}}(t) = \langle \vec{n}|\Psi^{\mathrm{FCI}}\rangle \tag{4}$$

are the complex time-dependent weights of each configuration's contribution to the many-body state $|\Psi^{\mathrm{FCI}}\rangle$. Here, and in the following, we drop the dependence on time for notational convenience. For bosons, there are

$$\binom{N+M-1}{N}$$

coefficients and for fermions, there are

$$\binom{M}{N}$$

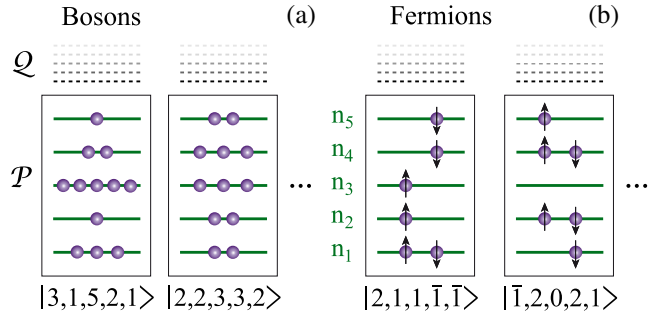

FIG. 1. Illustration of the configuration space of (a) MCTDH-B and (b) MCTDH-F. The space spanned by the time-dependent single-particle basis for which all configurations are considered is denoted by $\mathcal{P}$ and its complement is denoted by $\mathcal{Q}$. (a) For bosonic particles, the occupation numbers n_j are unrestricted, cf. the given five-orbital configuration vectors $|n_1, \ldots, n_5\rangle$. (b) For spin-1/2 fermions, the Pauli exclusion limits the occupations to be at most two electrons per spin orbital $n_j \leq 2$; see the given configurations ($\bar{1}$ [1] indicates a spin-down [-up] fermion).

coefficients. To obtain the EOMs, one can apply the time-dependent variational principle (Kramer and Saraceno, 2007) for the TDSE,

$$\hat{H}|\Psi\rangle = i\partial_t|\Psi\rangle, \tag{5}$$

and use $|\Psi^{\mathrm{FCI}}\rangle$ as an *Ansatz*. The action reads

$$S = \int dt \Big(\langle \Psi^{\mathrm{FCI}}|\hat{H} - i\partial_t|\Psi^{\mathrm{FCI}}\rangle - \sum_{kj} \mu_{kj}(t)[\langle \Phi_k|\Phi_j\rangle - \delta_{kj}] \Big). \tag{6}$$

The Lagrange multipliers $\mu_{kj}(t)$ ensure the orthonormalization of the single-particle states, $\langle \Phi_k|\Phi_j\rangle = \delta_{kj}$, at any time. We demand, independently, the stationarity of S with respect to variations of the orbitals $\{\Phi_i(\mathbf{r}, t)\}$ and the coefficients $\{C_{\vec{n}}(t)\}$,

$$\frac{\delta S[\{\Phi_i(\mathbf{r}; t)\}, \{C_{\vec{n}}(t)\}]}{\delta \Phi_i^*(\mathbf{r}; t)} \stackrel{!}{=} 0,$$
$$\frac{\delta S[\{\Phi_i(\mathbf{r}; t)\}, \{C_{\vec{n}}(t)\}]}{\delta C_{\vec{n}}^*(t)} \stackrel{!}{=} 0. \tag{7}$$

After a straightforward derivation (Caillat *et al.*, 2005; Alon, Streltsov, and Cederbaum, 2007c, 2008) we arrive at a coupled set of nonlinear coupled integrodifferential EOMs for the orbitals,

$$i\partial_t|\Phi_j\rangle = \hat{\mathbf{Q}} \Big[\hat{h}|\Phi_j\rangle + \sum_{k,s,q,l=1}^{M} \{\boldsymbol{\rho}\}_{jk}^{-1} \rho_{kslq} \hat{W}_{sl}(\mathbf{r}; t)|\Phi_q\rangle \Big],$$
$$\hat{\mathbf{Q}} = \mathbf{1} - \sum_i |\Phi_i\rangle\langle\Phi_i|. \tag{8}$$

In our derivation of this EOM we have, for convenience, set the gauge that removes the ambiguity in the choice of the orbitals (Meyer, Manthe, and Cederbaum, 1990; Manthe,

Meyer, and Cederbaum, 1992; Alon, Streltsov, and Cederbaum, 2007c, 2008) to be

$$\eta_{ij} = \langle \Phi_i | \partial_t \Phi_j \rangle = 0; \quad \forall \; i,j \in 1,\ldots,M. \tag{9}$$

Other choices for η_{ij} are possible (Manthe, 1994, 2015; Beck *et al.*, 2000; Caillat *et al.*, 2005). In particular, note here the choice for η_{ij} that forces the equations of motion to evolve natural orbitals (Manthe, 1994) as well as the choice for η_{ij} that entails optimal unoccupied orbitals (Manthe, 2015). The choice of the gauge affects the form of the MCTDH-X equations of motion and may thus provide some flexibility in designing the numerical approaches for the time integration of the EOMs, like splitting and regularization methods (Koch, Neuhauser, and Thalhammer, 2013; Lubich and Oseledets, 2014; Kloss, Burghardt, and Lubich, 2017; Lubich, Vandereycken, and Walach, 2018; Meyer and Wang, 2018).

In Eq. (8) we used the matrix elements of the reduced one-body and two-body density matrices,

$$\rho_{kq} = \langle \Psi | \hat{b}_k^\dagger \hat{b}_q | \Psi \rangle, \tag{10}$$

$$\rho_{kslq} = \langle \Psi | \hat{b}_k^\dagger \hat{b}_s^\dagger \hat{b}_l \hat{b}_q | \Psi \rangle, \tag{11}$$

respectively. Since these matrix elements, ρ_{kq} and ρ_{kslq}, are functions of the coefficients in the *Ansatz*, Eq. (2), the orbitals' time evolution is explicitly dependent on the coefficients' time evolution. The projector $\hat{\mathbf{Q}}$ in the EOMs emerges as a result of the elimination of the Lagrange multipliers μ_{kj} in the action S [Eq. (6)]; it is therefore a direct consequence of the orthonormalization of the orbitals $\Phi_j(\mathbf{r};t)$ at any time. In writing down Eq. (8), we further defined the local interaction potentials

$$\hat{W}_{sl}(\mathbf{r};t) = \int \Phi_s^*(\mathbf{r}';t)\hat{W}(\mathbf{r},\mathbf{r}';t)\Phi_l(\mathbf{r}';t)d\mathbf{r}'. \tag{12}$$

The EOMs for the coefficients [Eq. (4)] form a linear set of equations,

$$i\partial_t C_{\vec{n}}(t) = \sum_{\vec{n}'} \langle \vec{n};t|\hat{H}|\vec{n}';t\rangle C_{\vec{n}'}, \tag{13}$$

which is coupled to the orbital's EOMs [Eq. (8)] as the expectation value $\langle \vec{n};t|\hat{H}|\vec{n}';t\rangle$ is a function of the orbitals. This dependence on the orbitals can easily be understood by expressing the Hamiltonian in second-quantized notation:

$$\hat{H} = \sum_{k,q=1}^{M} h_{kq}\hat{b}_k^\dagger \hat{b}_q + \sum_{k,s,q,l=1}^{M} W_{ksql}\hat{b}_k^\dagger \hat{b}_s^\dagger \hat{b}_l \hat{b}_q. \tag{14}$$

Here the matrix elements of the one- and two-body Hamiltonian are, respectively,

$$h_{kq} = \langle \Phi_k | \hat{h}(\mathbf{r}_i;t) | \Phi_q \rangle, \tag{15}$$

$$W_{ksql} = \int d\mathbf{r} \int d\mathbf{r}' [\Phi_k(\mathbf{r};t)\Phi_s(\mathbf{r}';t) \times W(\mathbf{r},\mathbf{r}';t)\Phi_q(\mathbf{r};t)\Phi_l(\mathbf{r}';t)]. \tag{16}$$

The Hamiltonian, Eq. (14), is a function of h_{kq}, W_{ksql} that are, in turn, functions of the orbitals $\Phi_k(\mathbf{r};t)$. Therefore, the coefficients' time evolution, governed by the EOMs (8), also directly depends on the orbitals. The EOMs of the MCTDH-X method, Eqs. (8) and (13), are thus coupled.

B. Restricted spaces

Configurations can be removed from the full set employed in the *Ansatz* $|\Psi^{\mathrm{FCI}}\rangle$ [Eq. (2)] for the wave function that was used in the derivation of the MCTDH-X EOMs, Eqs. (8) and (13). This restriction of the configuration space reduces the numerical effort and may thus enable computations for cases where the number of terms in the *Ansatz* $|\Psi^{\mathrm{FCI}}\rangle$ is intractably large. Moreover, the changes in the emergent dynamics triggered by the restriction of the configuration space may lead to a physical insight into what parts of the Hilbert space are explored by the many-body state.

General restrictions to the configuration space are possible and lead to general MCTDH-X EOMs that have been discussed, for instance, by Haxton and McCurdy (2015) and Anzaki, Sato, and Ishikawa (2017). It is important to stress here that the MacLachlan (McLachlan, 1964) and Lagrangian (Kramer and Saraceno, 2007) variational principles, as well as their union, the Dirac-Frenkel variational principle (Swann, 1929; Dirac, 1930), lead to the same unified MCTDH-X EOMs only in the case in which the *Ansatz* for the wave function contains all possible configurations, i.e., as given in Eq. (2). For general *Ansätze* with a restricted set of configurations, however, the McLachlan and Lagrangian variational principles can be inequivalent (Haxton and McCurdy, 2015).

Here we focus on the RAS approach for the restriction of the configuration space (Olsen *et al.*, 1988) of MCTDH-X, because we find its strategy for the construction of many-body Hilbert space instructive and suitable to illustrate the changes that arise when one deals with a truncated configuration space. Moreover, there are applications of the RAS approach in combination with MCTDH-X for both bosons and fermions. In the literature, these methods are referred to as time-dependent RAS self-consistent-field (TD-RASSCF) for fermions (TD-RASSCF-F) (Miyagi and Madsen, 2013, 2014a, 2014b) and TD-RASSCF-B for bosons (Lévêque and Madsen, 2017, 2018). For clarity and coherence of presentation in this Colloquium, we refer to TD-RASSCF-F and TD-RASSCF-B as RAS-MCTDH-B and RAS-MCTDH-F, respectively, and RAS-MCTDH-X together.

We note here the conceptual similarities of RAS-MCTDH-X and the time-dependent occupation-restricted multiple-active-space theory mentioned by Sato and Ishikawa (2015).

In the original formulation of the RAS-MCTDH-F (Miyagi and Madsen, 2013, 2014b), three subspaces of adaptive orbitals were considered: $\mathcal{P}_0$, $\mathcal{P}_1$, and $\mathcal{P}_2$ with M_0 frozen, M_1 unrestricted, and M_2 restricted orbital occupations, respectively. The $\mathcal{P}_0$ space with orbitals with frozen occupations is hard to define for bosons. For simplicity we limit ourselves here to the case of RAS-MCTDH-X with two active subspaces, $\mathcal{P}_1$ and $\mathcal{P}_2$, to restrict the number of configurations with a total number $M = M_1 + M_2$ orbitals. The number of orbitals in the $\mathcal{P}_1$ subspace must be large enough to accommodate all the particles, i.e., one configuration, at least, has no particles in the $\mathcal{P}_2$ subspace. For bosons, the $\mathcal{P}_1$ subspace

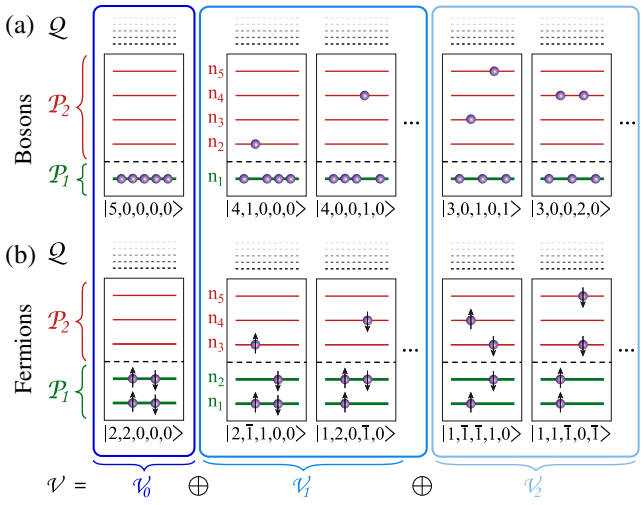

FIG. 2. Illustration of restricted active space schemes for the restriction of configuration spaces for (a) bosons and (b) fermions. The space of active orbitals is partitioned into two sets $\mathcal{P}_{1,2}$ and the space of virtual orbitals is denoted by $\mathcal{Q}$. All possible configurations of N particles in the M_1 orbitals of the $\mathcal{P}_1$ space are considered in the *Ansatz* of RAS-MCTDH-X. For the $\mathcal{P}_2$ space, a maximal occupation of all M_2 orbitals together is fixed to be $N_{\max}$. Thus, in RAS-MCTDH-X, of all possible configurations of N particles in $\mathcal{P}_1 \oplus \mathcal{P}_2$, those configurations where there are more than $N_{\max}$ particles in $\mathcal{P}_2$ are dropped. The total Hilbert space $\mathcal{V}$ spanned by the *Ansatz* of RAS-MCTDH-X (17) is a direct sum of the subspaces that contain $0, \ldots, N_{\max}$ particles (blue boxes labeled $\mathcal{V}_1, \mathcal{V}_2, \ldots$).

includes at least one orbital and for fermions $M_1 \geq N$ holds. The restriction on the configuration space follows from specifying a maximum number of particles $N_{\max}$ that can occupy the $\mathcal{P}_2$ subspace. The *Ansatz* for the RAS-MCTDH-X method reads

$$|\Psi^{\mathrm{RAS}}\rangle = \sum_{\vec{n}\in\mathcal{V}} C_{\vec{n}}(t)|\vec{n},t\rangle, \tag{17}$$

where the configurations span the space $\mathcal{V}$ that is obtained by restricting the total configurational space of Eq. (2) using the RAS determined through the parameters M_1, M_2, and $N_{\max}$. See Fig. 2 for an illustration of the RAS-MCTDH-X configuration space and the ansatz in Eq. (17).

The RAS-MCTDH-X wave function can be seen as a bridge between the mean-field approaches, TD Hartree-Fock for fermions and TD Gross-Pitaevskii for bosons on one end, and the MCTDH-X approach on the other end: all are limiting cases of the RAS-MCTDH-X *Ansatz*. The EOMs for the set of time-dependent coefficients $\{C_{\vec{n}}(t)\}$ and orbitals $\{|\Phi_i(t)\rangle\}_{i=1}^{M}$ are derived following the recipes of the MCTDH-X framework, see Sec. II.A, albeit here with a real (Lagrangian) action functional (Miyagi and Madsen, 2013, 2014b; Lévêque and Madsen, 2017). A set of equations for the coefficients and the orbitals is obtained,

$$i\partial_t C_{\vec{n}} = \sum_{ij}(h_{ij} - i\eta_{ij})\langle\Phi_{\vec{n}}|\hat{b}_i^\dagger\hat{b}_j|\Psi\rangle + \frac{1}{2}\sum_{ijkl} W_{ikjl}\langle\Phi_{\vec{n}}|\hat{b}_i^\dagger\hat{b}_k^\dagger\hat{b}_l\hat{b}_j|\Psi\rangle, \tag{18}$$

and

$$i\hat{\mathbf{Q}}[\partial_t|\Phi_j\rangle] = \hat{\mathbf{Q}}\left[\hat{h}|\Phi_j\rangle + \sum_{k,s,q,l=1}^{M}\{\boldsymbol{\rho}\}^{-1}_{jk}\rho_{kslq}\hat{W}_{sl}(\mathbf{r};t)|\Phi_q\rangle\right], \tag{19}$$

respectively. The set of equations for the orbitals is similar to the one obtained for MCTDH-X, see Eq. (8), except that the projector $\hat{\mathbf{Q}}$ appears on both sides of Eq. (19) and the set of equations for the coefficients includes an additional term, namely, $\eta_{ij} = \langle\Phi_i|\dot{\Phi}_j\rangle$. This gauge freedom, typically set to zero in the MCTDH-X equations, cannot be chosen arbitrarily to simplify the equations of RAS-MCTDH-X any more, because the $\mathcal{P}_1$ and $\mathcal{P}_2$ orbitals are not equivalent and the transformation of the orbitals from one subspace to another has to be taken into account explicitly. Thus, for each pair of orbitals $\{\Phi_{i'}, \Phi_{j''}\}$, with $\Phi_{i'} \in \mathcal{P}_1$ and $\Phi_{j''} \in \mathcal{P}_2$, the matrix element $\eta_{i'j''}$ is evaluated via an additional set of equations. The choice of the excitation scheme to promote particles from the $\mathcal{P}_1$ to the $\mathcal{P}_2$ subspace plays an important role to simplify the evaluation of $\eta_{i'j''}$. Here we present the case of the so-called general excitation scheme (Miyagi and Madsen, 2014b), where all successive occupation numbers $0, \ldots, N_{\max}$ of the $\mathcal{P}_2$ subspace are considered. The matrix elements $\eta_{i'j''}$ are evaluated from

$$\sum_{k''l'}(i\eta_{k''l'} - h_{k''l'})\zeta^{l'j''}_{k''i'} = \frac{1}{2}\sum_{klmn} W_{kmln}\zeta^{lnj''}_{kmi'}, \tag{20}$$

where the fourth- and sixth-order tensors are defined by

$$\zeta^{l'j''}_{k''i'} = \langle\Psi|\hat{b}_{i'}^\dagger\hat{b}_{j''}(\hat{1} - \hat{\Pi})\hat{b}_{k''}^\dagger\hat{b}_{l'}|\Psi\rangle, \tag{21}$$

$$\zeta^{lnj''}_{kmi'} = \langle\Psi|\hat{b}_{i'}^\dagger\hat{b}_{j''}(\hat{1} - \hat{\Pi})\hat{b}_k^\dagger\hat{b}_m^\dagger\hat{b}_n\hat{b}_l|\Psi\rangle, \tag{22}$$

with

$$\hat{\Pi} = \sum_{\vec{n}\in\mathcal{V}}|\vec{n},t\rangle\langle\vec{n},t|$$

being the projector onto the RAS configurations. The time derivative of the orbitals can be expressed as

$$\partial_t|\Phi_j\rangle = \sum_i \eta_{ij}|\Phi_i\rangle + \hat{\mathbf{Q}}[\partial_t|\Phi_j\rangle].$$

The $\eta_{ij}|\Phi_i\rangle$ term describes the transformation of the $\mathcal{P}_1$ and $\mathcal{P}_2$ orbitals into each other, and the $\hat{\mathbf{Q}}[\partial_t|\Phi_j\rangle]$ term describes the extension of the time-evolved orbitals into the space not spanned by the orbitals at time t. From Eqs. (20) and (19) the time derivative of the orbitals can be evaluated, and from Eq. (18) the time derivatives of the coefficients are available after solving Eq. (20) for the matrix elements $\eta_{i'j''}(t)$. The restriction of the configuration space thus leads to more complicated EOMs, but the drastic reduction of the number of configurations enables faster or in some situations more accurate descriptions of many-body systems than plain

MCTDH-X. Note that the EOMs for other RAS-excitation schemes can be found in Miyagi and Madsen (2013, 2014b) and Lévêque and Madsen (2017). For the so-called complete active space approach with an additional space hosting orbitals with occupations that are fixed, see Sato and Ishikawa (2015).

C. Benchmarks with an exactly solvable model

Since the introduction of MCTDH-B and MCTDH-F, many benchmarks of the predictions of these approaches have been performed. Most of these benchmarks consist in a comparison of the predictions of the MCTDH-X approaches to other theoretical approaches like, for instance, exact diagonalization with a time-independent one-particle basis set. Such example benchmarks against other approaches include the ionization of helium-4 (Hochstuhl and Bonitz, 2011) or the photoionization of beryllium-9 (Haxton, Lawler, and McCurdy, 2011) in the case of MCTDH-F or a comparison with the Bose-Hubbard model (Streltsov, Alon, and Cederbaum, 2006; Sakmann *et al.*, 2009) in the case of MCTDH-B. We note that the interesting MCTDH-X applications are those cases where diagonalization is no longer affordable numerically. We note also the benchmark of MCTDH-B for the exactly solvable problem of two bosons with contact interactions in a harmonic trap (Gwak, Marchukov, and Fischer, 2018). Here, we focus on available benchmarks of MCTDH-X with exactly solvable models, specifically, on the harmonic interaction model (HIM) (Cohen and Lee, 1985; Załuska-Kotur *et al.*, 2000; Yan, 2003; Gajda, 2006; Armstrong *et al.*, 2011) that describes N indistinguishable harmonically trapped particles interacting via a harmonic interaction potential that is proportional to the square of their distance. The HIM has the unique feature that it straightforwardly can be generalized to include time dependence in the harmonic trapping of and the harmonic interactions between particles while remaining exactly solvable (Lode, Sakmann *et al.*, 2012; Lode, 2015; Fasshauer and Lode, 2016). This time-dependent HIM (TD-HIM) is a well-suited test case for MCTDH-X, because it represents one of the rare cases where a numerically exact solution to the TDSE for a correlated problem with a time-dependent Hamiltonian can be obtained. The solution is achieved via a mapping to a time-dependent one-body Schrödinger equation that can be integrated numerically at any desired level of accuracy with little effort.

The Hamiltonian of the TD-HIM reads

$$\hat{H}_{\mathrm{TDHIM}}(t)=\sum_{i=1}^{N}\left(-\frac{1}{2}\partial_{\mathbf{r}}^{2}+\frac{1}{2}\omega_{\mathrm{TD}}(t)^{2}\mathbf{r}^{2}\right)+K_{\mathrm{TD}}(t)\sum_{i<j}^{N}(\mathbf{r}_{i}-\mathbf{r}_{j})^{2}, \tag{23}$$

where the time-dependent trap frequency ω_{TD} and the time-dependent interaction strength K_{TD} are given by

$$\omega_{\mathrm{TD}}(t)=\omega[1+f(t)], \quad K_{\mathrm{TD}}(t)=K\left[1-\frac{\omega_{0}^{2}}{2NK}f(t)\right]. \tag{24}$$

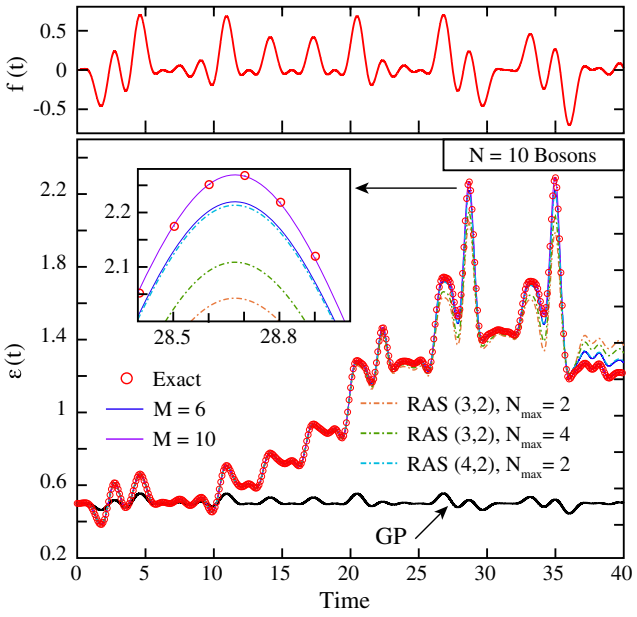

FIG. 3. Benchmark of (RAS-)MCTDH-B against exact TD-HIM results for $N=10$ bosons. Here we use $f(t)=\sin(t)\cos(2t)\sin(0.5t)\sin(0.4t)$ (upper panel) and $K=0.5$ in Eqs. (23) and (24). The time-dependent center-of-mass energy $\varepsilon(t)$ (solid and dashed lines for MCTDH-B and RAS-MCTDH-B results, respectively) is plotted in comparison to the exact values (circles) in the lower panel for different particle and orbital numbers [see Lode, Sakmann *et al.* (2012) for details on $\varepsilon(t)$]. A convergence with an increasing number of orbitals, i.e., amount of variational parameters in the (RAS-)MCTDH-B wave function, is observed.

We compare solutions of the TDSE with this Hamiltonian to (RAS-)MCTDH-B ones in Fig. 3.

The convergence of (RAS-)MCTDH-B toward the exact result for an increasing number of variational parameters in the wave function is demonstrated by the results in Fig. 3 for $N=10$ bosons; for a demonstration with fermions and MCTDH-F see Fasshauer and Lode (2016).

III. MCTDH-B AND BOSE-EINSTEIN CONDENSATES

For brevity, we restrict our discussion here to the quantum dynamics obtained with MCTDH-B modeling an experiment with a quasi-one-dimensional BEC subject to a time-dependent interparticle interaction in Sec. III.B as well as to the appealing many-body physics in the variance of observables in Sec. III.C. Before turning to these applications of MCTDH-B, we introduce the relevant quantities of interest.

A. Analyzing many-body states of bosons

The key insight that MCTDH-B has to offer is due to the fact that it is a wave-function-based approach: from the approximate solution $|\Psi(t)\rangle$ to the TDSE, correlations and coherence can be quantified, for instance, using *reduced density matrices* and their eigenvalues (Sakmann *et al.*, 2008):

$$\rho^{(p)}(\mathbf{r}_1,\ldots,\mathbf{r}_p,\mathbf{r}'_1,\ldots,\mathbf{r}'_p;t) = \mathrm{Tr}_{p+1,\ldots,N}[|\Psi(t)\rangle\langle\Psi(t)|] = \frac{N!}{(N-p)!}\int d\mathbf{r}_{p+1}\cdots d\mathbf{r}_N \Psi^*(\mathbf{r}'_1,\ldots,\mathbf{r}'_p,\mathbf{r}_{p+1},\ldots,\mathbf{r}_N;t) \times \Psi(\mathbf{r}_1,\ldots,\mathbf{r}_p,\mathbf{r}_{p+1},\ldots,\mathbf{r}_N;t). \quad (25)$$

The diagonal of the pth-order density matrix, i.e., $\rho^{(p)}(\mathbf{r}_1,\ldots,\mathbf{r}_p,\mathbf{r}_1,\ldots,\mathbf{r}_p;t) \equiv \rho^{(p)}(\mathbf{r}_1,\ldots,\mathbf{r}_p;t)$, is the probability to find particles $1,\ldots,p$ at positions $\mathbf{r}_1,\ldots,\mathbf{r}_p$, respectively, and is referred to as the p-body density. In the case of $p=1$, by convention, one drops the (1) superscript and speaks of just the density $\rho(\mathbf{r};t)$, i.e., $\rho(\mathbf{r};t) \equiv \rho^{(1)}(\mathbf{r};t) \equiv \rho^{(1)}(\mathbf{r},\mathbf{r}'=\mathbf{r};t)$ is implied. In this section, we present observables like $\rho^{(p)}$ derived using the wave function $|\Psi(t)\rangle$ in position space; the equations are, however, also valid for momentum space analogons of the observables when the wave function in momentum space is used and $\mathbf{r}$ is replaced by $\mathbf{k}$. The off-diagonal part of the pth-order reduced density matrix $\rho^{(p)}(\mathbf{r}'_1\neq\mathbf{r}_1,\ldots,\mathbf{r}'_p\neq\mathbf{r}_p,\mathbf{r}_1,\ldots,\mathbf{r}_p;t)$ determines the pth-order coherence. To further quantify the pth-order coherence, the pth-order Glauber correlation function

$$g^{(p)}(\mathbf{r}_1,\ldots,\mathbf{r}_p,\mathbf{r}'_1,\ldots,\mathbf{r}'_p;t) = \frac{\rho^{(p)}(\mathbf{r}_1,\ldots,\mathbf{r}_p,\mathbf{r}'_1,\ldots,\mathbf{r}'_p;t)}{\sqrt{\prod_{k=1}^{p}[\rho^{(1)}(\mathbf{r}_k;t)\rho^{(1)}(\mathbf{r}'_k;t)]}} \quad (26)$$

is a good measure. Essentially, $g^{(p)}$ gives a spatially resolved picture of the representability of the pth-order density matrix by a product of one-body densities: $g^{(p)}\neq 1$ implies that the p-body density cannot be represented by a product of one-body densities. In this $g^{(p)}\neq 1$ case, therefore, the many-body state contains quantum correlations (of pth order). Such quantum correlations entail fluctuations of observables and can be probed (experimentally) with single-shot images or via the variance of operators (see later).

One important correlation effect that has been discussed in many works applying MCTDH-B is fragmentation (Nozieres and St. James, 1982; Spekkens and Sipe, 1999; Mueller *et al.*, 2006), i.e., the situation when the reduced one-body density matrix $\rho^{(1)}(\mathbf{r},\mathbf{r}';t)$ of interacting bosons acquires several macroscopic eigenvalues (Streltsov, Alon, and Cederbaum, 2008, 2009, 2011; Sakmann *et al.*, 2009, 2010; Sakmann, 2011; Lode, Streltsov *et al.*, 2012; Lode, 2015, 2016; Lode and Bruder, 2017). If $\rho^{(1)}(\mathbf{r},\mathbf{r}';t)$ has only one single significant eigenvalue, then the state is referred to as condensed (Penrose and Onsager, 1956).

To discuss fragmentation and condensation, we thus write $\rho^{(1)}(\mathbf{r},\mathbf{r}';t)$ using its eigenvalues $n_i^{(1)}(t)$ and its eigenfunctions $\Phi_i^{(\mathrm{NO})}(\mathbf{r};t)$:

$$\rho^{(1)}(\mathbf{r},\mathbf{r}';t) = \sum_i n_i^{(1)}(t)\Phi_i^{(\mathrm{NO}),*}(\mathbf{r}';t)\Phi_i^{(\mathrm{NO})}(\mathbf{r};t). \quad (27)$$

We note that the $n_i^{(1)}(t)$ are nothing but the eigenvalues of the matrix elements $\rho_{kq}(t)$ in Eq. (10). In practice, the $n_i^{(1)}(t)$ are therefore computed by straightforwardly diagonalizing the $M\times M$ matrix $\rho_{kq}(t)$. Analogously, the eigenvalues $n_i^{(2)}(t)$ of the two-body density $\rho^{(2)}$ are available via the diagonalization of $\rho_{kslq}(t)$.

In cold-atom experiments, the standard measurement is absorption images. Such *single-shot images* correspond to a projective measurement of the many-body state $|\Psi\rangle$ (Javanainen and Yoo, 1996; Castin and Dalibard, 1997; Dziarmaga, Karkuszewski, and Sacha, 2003; Sakmann and Kasevich, 2016). In the ideal case, each image contains information about the position or momentum of every particle. Each measurement thus corresponds to a random sample $\mathbf{s}^k$ of positions that is distributed according to the N-body probability distribution

$$P(\mathbf{r}_1,\ldots,\mathbf{r}_N;t) = \rho^{(N)}(\mathbf{r}_1,\ldots,\mathbf{r}_N;t) = |\Psi(\mathbf{r}_1,\ldots,\mathbf{r}_N;t)|^2$$

$$\mathbf{s}^k = \{\mathbf{s}_1^k,\ldots,\mathbf{s}_N^k\} \sim |\Psi(\mathbf{r}_1,\ldots,\mathbf{r}_N;t)|^2. \quad (28)$$

To directly model these images with a wave function computed by MCTDH-X, one has to draw random samples from the N-body density, i.e., compute a set of so-called single-shot simulations s^k, $k=1,\ldots,N_{\mathrm{shots}}$. The numerical difficulty in sampling high-dimensional probability distributions can be overcome by factorizing the N-particle probability into a set of conditional probabilities,

$$P(\mathbf{r}_1,\ldots,\mathbf{r}_N;t) = P(\mathbf{r}_1;t)P(\mathbf{r}_2|\mathbf{r}_1;t)\times\cdots \times P(\mathbf{r}_N|\mathbf{r}_1,\ldots,\mathbf{r}_{N-1};t). \quad (29)$$

To obtain a simulation $\mathbf{s}=(s_1,\ldots,s_N)$ of a single shot, the first particle's position s_1 is drawn from the one-body density

$$s_1 \sim P(\mathbf{r};t) = \rho(\mathbf{r};t) = \langle\Psi|\hat{\Psi}^\dagger(\mathbf{r};t)\hat{\Psi}(\mathbf{r};t)|\Psi\rangle. \quad (30)$$

Here,

$$\hat{\Psi}(\mathbf{r}) = \sum_{j=1}^{M}\hat{b}_j\Phi_j(\mathbf{r};t)$$

is the field annihilation and

$$\hat{\Psi}^\dagger(\mathbf{r}) = \sum_{j=1}^{M}\hat{b}_j^\dagger\Phi_j^*(\mathbf{r};t)$$

the field creation operator. The second particle's position s_2 is then sampled from the conditional probability that is computed from a reduced many-body state $\Psi^{(1)}$, where a particle has been detected at s_1,

$$s_2 \sim P(\mathbf{r}_2|s_1;t) = \langle\Psi^{(1)}|\hat{\Psi}^\dagger(\mathbf{r};t)\hat{\Psi}(\mathbf{r};t)|\Psi^{(1)}\rangle, \quad |\Psi^{(1)}\rangle = \mathcal{N}^{(1)}\hat{\Psi}(s_1)|\Psi\rangle. \quad (31)$$

Here, $\mathcal{N}^{(1)}$ represents some normalization constant. This procedure is continued until all particles have been detected at positions $s_1,\ldots,s_N$ and the single-shot image, i.e., the

vector of positions $\mathbf{s} = (s_1, \ldots, s_N)$, is obtained. In principle, all information about the N-body density $\rho^{(N)}(\mathbf{r}_1, \ldots, \mathbf{r}_N; t)$ can be extracted from single-shot images.

We now discuss the variances of observables that are sums of one-body operators $\hat{A} = \sum_{i=1}^{N} \hat{a}(\mathbf{r}_i)$:

$$\frac{1}{N}\Delta_{\hat{A}}^2 = \frac{1}{N}(\langle \hat{A}^2 \rangle - \langle \hat{A} \rangle^2). \tag{32}$$

Formally, two-particle operators contribute to the value of this variance, because of the $\hat{A}^2$ term in Eq. (32),

$$\hat{A}^2 = \sum_{j=1}^{N} \hat{a}^2(\mathbf{r}_j) + \sum_{k>j=1}^{N} 2\hat{a}(\mathbf{r}_j)\hat{a}(\mathbf{r}_k). \tag{33}$$

Using the one-body and two-body reduced density matrices [Eq. (25)] to evaluate Eq. (32), we obtain

$$\frac{1}{N}\Delta_{\hat{A}}^2 = \int d\mathbf{r} \frac{\rho(\mathbf{r})}{N} a(\mathbf{r})^2 - N\left[\int d\mathbf{r} \frac{\rho(\mathbf{r})}{N} a(\mathbf{r})\right]^2 + \int d\mathbf{r}_1 d\mathbf{r}_2 \frac{\rho^{(2)}(\mathbf{r}_1, \mathbf{r}_2, \mathbf{r}_1, \mathbf{r}_2)}{N} a(\mathbf{r}_1)a(\mathbf{r}_2). \tag{34}$$

Evidently, the operator $\hat{A}^2$ [Eq. (33)] and the variance $\Delta_{\hat{A}}^2$ thus depend on the coordinates of two particles and are, thereby, two-body operators that can be used to probe many-body physics. In Eq. (34), one-body operators that are local in position space $[\hat{a}(\mathbf{r})]$ are considered; a generalized form of Eq. (34) has been found, for instance, by Alon (2019a). Typical choices for $\hat{A}$, which we discuss in Sec. III.C, include the many-body position and momentum operators, $\hat{X} = \sum_{i=1}^{N} \hat{x}_i$ and $\hat{P} = \sum_{i=1}^{N} \hat{p}_i$.

B. Quantum fluctuations and correlations in systems of ultracold bosons

Faraday waves and "granulation" of a BEC driven with a modulated interparticle interaction strength have been observed in a recent experiment in a quasi-one-dimensional setup at Rice University (Nguyen *et al.*, 2019).

Faraday waves result for modulation frequencies on or close to resonance with the transversal trapping (Faraday, 1830) even at rather small-amplitude modulations: Faraday waves are regular, standing, periodic patterns, seen for instance in liquids in a vessel that is shaken. In experimental realizations, the single-shot images of Faraday waves are repeatable (Engels, Atherton, and Hoefer, 2007; Nguyen *et al.*, 2019).

Granulation (Yukalov, Novikov, and Bagnato, 2014, 2015; Nguyen *et al.*, 2019) results for larger-amplitude modulations with frequencies much lower than the radial confinement: the BEC breaks into "grains" of varying size. The sizes of these grains are broadly distributed, and the grains persist for up to *four seconds*, i.e., much longer than the modulation time. In the experimental realization, the single-shot images of the granular state, as a direct consequence of quantum correlations and fluctuations, were different, even if all parameters in the experiment were kept fixed (Nguyen *et al.*, 2019).

We stress that the presence of quantum fluctuations and correlations in a many-body state cannot be inferred from the density alone. Models like the time-dependent Gross-Pitaevskii mean-field or the time-dependent density functional theory that—*a priori*—by the construction of their *Ansatz*, are aimed at the density may therefore not be able to describe quantum fluctuations and correlations accurately.

A statistical analysis of many observations of the quantum state, i.e., of many (simulated) absorption images in the case of ultracold atoms, is needed in order to study and precisely quantify effects like quantum correlations and fluctuations.

Here, we focus on the case where granulation emerges in the BEC, since the quantum correlations and fluctuations that arise in sync with granulation make this a good example where the application of a wave-function-based theory like MCTDH-B is crucial, because MCTDH-B (and also MCTDH-F) does incorporate quantum correlations in its *Ansatz* [cf. Eq. (2)]. Moreover, the experimental observations in single-shot images can also directly be obtained from the MCTDH-B simulations.

Such a direct comparison of single-shot images simulated from MCTDH-B-computed wave functions with the experimental observations on granulation was performed by Nguyen *et al.* (2019). The one-body Hamiltonian used to model the granulation experiment was

$$\hat{h}(x) = -\frac{1}{2}\frac{\partial^2}{\partial x^2} + \frac{1}{2}\Omega^2 x^2,$$

i.e., a kinetic energy term and a parabolic trap in dimensionless units—the total Hamiltonian was divided by $\hbar^2/mL^2$, where m is the mass of ^{7}Li and a length scale L such that $\Omega \approx 0.1$; see Nguyen *et al.* (2019) for details. The time-dependent interaction potential was modeled as

$$W(x, x'; t) = \lambda(t)\delta(x - x'), \tag{35}$$

where

$$\lambda(t) = \lambda_0\left[-\beta_1 + \frac{\beta_1}{\beta_2 - \beta_3 \sin(\omega t)}\right]$$

is the time-dependent interaction strength. Here $\beta_2 = |(\bar{B} - B_\infty)/\Delta|$, $\beta_1 = -\beta_2/(\beta_2 - 1) = 3.10$, and $\beta_3 = |\Delta B/\Delta|$ are the parameters of the applied time-dependent magnetic field $B(t) = \bar{B} + \Delta B \sin(\omega t)$, where $B_\infty = 736.8$ G, $\bar{B} = 590.9$ G, and $\Delta = 192.3$ G. Importantly, the sinusoidal modulation of the magnetic field creates a periodic but *nonsinusoidal* modulation of the interparticle interaction strength $\lambda(t)$.

The MCTDH-B-simulated and the experimental single-shot images do qualitatively agree; see Figs. 4(a) and 4(b).

In our present example of the granulation of a BEC, a contrast parameter $\mathcal{D}$ that measures discrepancies by more than 20% of experimental and simulated single-shot images from a Thomas-Fermi profile was defined to quantify the amount of fluctuations in the many-body system; see Fig. 4(c).

Since there is no evidence for thermal effects in the experimental realization of granulation, the observed fluctuations are necessarily attributed to quantum correlations.

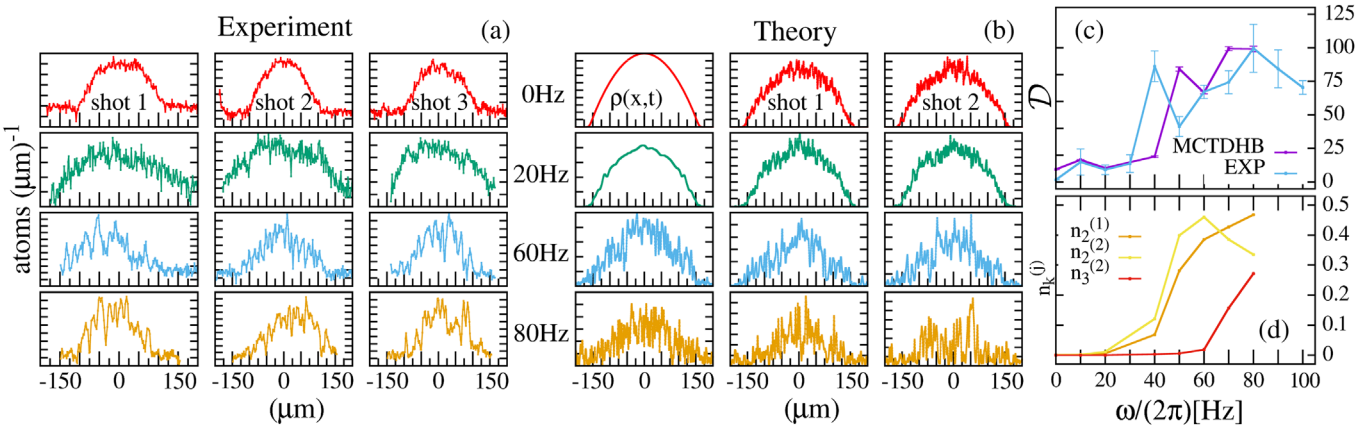

FIG. 4. Experimental and theoretical single-shot line density profiles. (a) Experimental data and (b) many-body simulations for different modulation frequencies. (a) The rows show data for three independent experimental images (single shots) for the indicated ω, where $\omega = 0$ Hz corresponds to no modulation. The interaction between particles was modulated for $t_m = 250$ ms around an average value of $8a_0$ with a maximum of $20a_0$ and a minimum of $0.7a_0$; subsequently, the interactions are held constant for another $t_h = t_m = 250$ ms. (b) The first column shows the density $\rho(z,t)$ [Eq. (25) for $p = 1$, $\mathbf{r}_1 = \mathbf{r}_1' = z$] as calculated from the one-dimensional MCTDH-B computations, while the second and third columns display two simulated single-shot images [Eq. (28)]. We observe that granulation is present in single-shot images, but absent in the average $\rho(z,t)$. Quantum fluctuations characterize the emergence of granulation: (c) Comparison of the deviations from a Thomas-Fermi distribution as quantified by the contrast parameter $\mathcal{D} = \mathcal{D}(\omega)$ [see Nguyen *et al.* (2019) for details about $\mathcal{D}$] for single shots simulated from wave functions computed with MCTDH-B (line with smaller error bars) and single shots taken in experiment (EXP, line with larger error bars). MCTDH-B predicts the threshold value $\omega_c \approx (2\pi)30$ Hz, where deviations become large and grains form. Each symbol and its error bar are the mean and standard error of the mean of at least four experimental measurements of $\mathcal{D}$, while 100 single shots at each ω have been simulated from the MCTDH-B wave functions. (d) Eigenvalues of the first- and second-order reduced density matrices. A growth of $n_2^{(1)}$, $n_2^{(2)}$, and $n_3^{(2)}$ (upper, middle, and lower lines at $\omega/2\pi = 50$ Hz, respectively) is observed to occur for $\omega > \omega_c$, indicating the emergence of correlations and fragmentation. The growths of both $n_2^{(1)}$ and $n_2^{(2)}$ occur as $\omega \approx \omega_c$, with the drop in $n_2^{(2)}$ near 60 Hz corresponding to the subsequent growth in $n_3^{(2)}$. Adapted from Figs. 7 and 9 of Nguyen *et al.*, 2019.

From the contrast parameter [Fig. 4(c)], we understand that granulation emerges beyond modulation frequencies of $\omega_c \approx (2\pi)30$ Hz and appears side by side with quantum correlations, as seen from a significant growth of multiple eigenvalues of the one-body and two-body density matrices; see Fig. 4(d).

The agreement between the contrast parameter obtained from experimental and simulated single-shot simulations [Fig. 4(c)] heralds the reliability of the MCTDH-B prediction for the many-body wave function and the quantum correlations and fluctuations embedded in it.

C. Many-body physics and variances

The interconnection between mean-field and many-body descriptions of a BEC has attracted considerable attention (Calogero and Degasperis, 1975; Nozieres and St. James, 1982). Whereas the Gross-Pitaevskii theory has widely been employed in earlier investigations (Edwards and Burnett, 1995; Burger *et al.*, 1999), there is nowadays a growing consensus of the need for models that go beyond mean field, as highlighted in Sec. III.B.

Exact and appealing relations between many-body and mean-field descriptions of ultracold bosons are obtained in the so-called infinite-particle-number limit (IPNL), i.e., in the limit where the product of the interaction strength and the number of particles N is kept fixed while the number of particles tends to infinity (Castin and Dum, 1998; Lieb, Seiringer, and Yngvason, 2000; Lieb and Seiringer, 2002; Erdős, Schlein, and Yau, 2007a, 2007b; Cederbaum, 2017). In this IPNL, the energy and density per particle E/N and $\rho(\mathbf{r})/N$, respectively, of the BEC computed at the many-body and mean-field levels of theory for $N \to \infty$ are equal; the BEC is 100% condensed.

The Gross-Pitaevskii mean-field theory is obtained as the limiting case when only a single orbital is used with MCTDH-B and computations for a large number of bosons can be done with (RAS-)MCTDH-B, in particular, when the considered state is almost 100% condensed. MCTDH-B is thus well suited to investigate the interconnection between mean-field and many-body descriptions in the IPNL; we focus on some of the pertinent applications of MCTDH-B in the following discussion.

Even in the IPNL, however, correlations are embedded within a BEC and show in the variance of operators. For the position operator $\hat{X} = \sum_{j=1}^{N} \hat{x}_j$, where $\hat{x}_j$ is the position of the jth particle, the effect of correlations can be clearly seen in its variance

$$\frac{1}{N}\Delta^2_{\hat{X}} = \frac{1}{N}(\langle \hat{X}^2 \rangle - \langle \hat{X} \rangle^2),$$

see Eq. (33) and Klaiman and Alon (2015) and Klaiman, Streltsov, and Alon (2016). The reason is that an excitation of as little as a fraction of a particle outside the condensed mode may interact with a macroscopic number of particles in the condensed mode. Formally, two-particle operators contribute

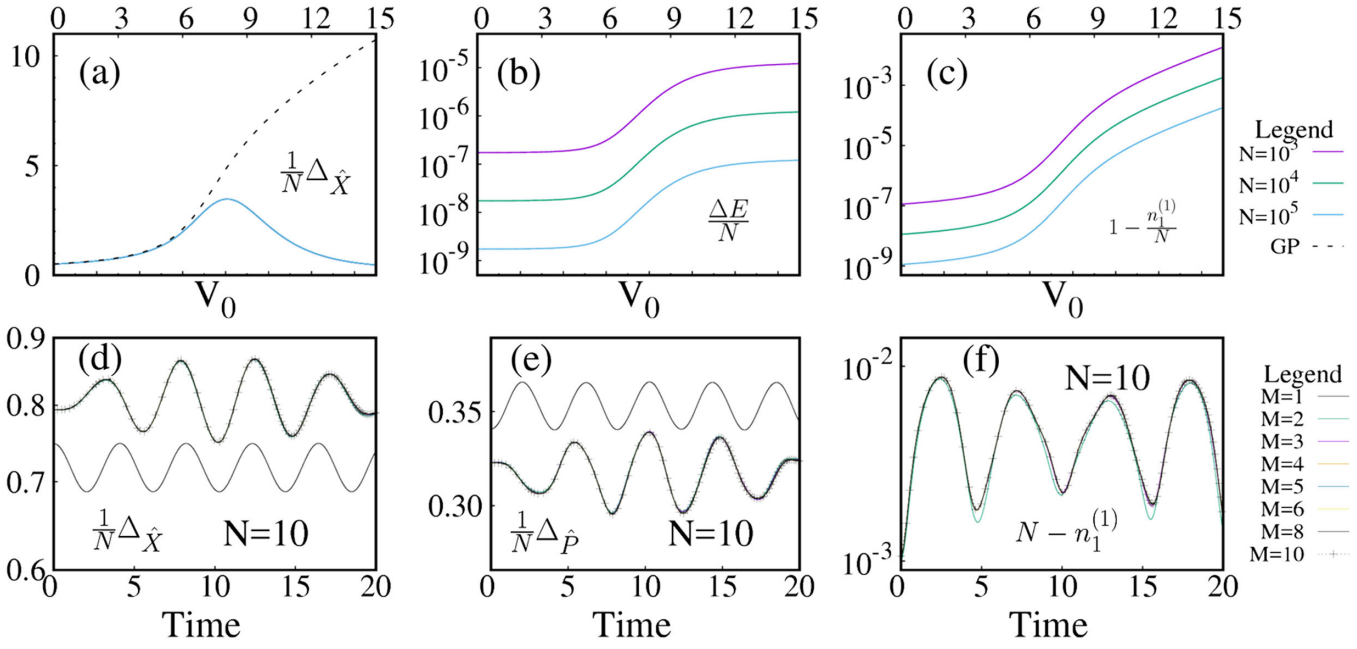

FIG. 5. The position space variance (a) of $N = 1000$, 10 000, and 100 000 bosons with contact interactions such that $\Lambda = \lambda(t)(N-1) = 0.1$ in a double well as a function of the barrier height on the many-body level (three colored or gray lines atop of each other) drastically differs from the mean-field description (black-dashed line), although the energy per particle in (b) and depletion in (c) suggest that a mean-field description is applicable (solid lines from top to bottom for $N = 1000$, 10 000, and 100 000, respectively); see also Fig. 1 of Klaiman and Alon (2015). The position variance per particle in (d), momentum variance per particle in (e), and number of depleted particles in (f) for the dynamics of $N = 10$ attractive bosons in an anharmonic trap $V(x) = 0.05x^4$. The dynamics follow a quench of the strength of the interactions [attractive Gaussian interaction potential $\lambda(t)e^{0.5(x-x')^2}$ with $\lambda(t) = -0.02$ for $t < 0$ and $\lambda(t) = -0.04$ for $t \geq 0$]. (d)–(f) Replotted with data from Fig. 6 in Alon and Cederbaum (2018). A smaller distance from the exact result ($M = 10$, crosses) of the lines in (d)–(f) for different orbital number M indicates larger M (values of M in the legend): convergence with M is found.

to the evaluation of the variance of one-particle operators; cf. Eq. (33). This is an intriguing result, in particular, because the state is 100% condensed at the IPNL, i.e., the reduced one-particle and two-particle density matrices per particle, $\rho^{(1)}/N$ and $\rho^{(2)}/[N(N-1)]$ [Eq. (25) for $p = 1, 2$], respectively, do have only a single macroscopic eigenvalue. In practice, one thus finds a difference when the variance is computed at the many-body and mean-field levels; see Figs. 5(a)–5(c) for an example with $(1/N)\Delta^2_{\hat{X}}$ for bosons in a double well. This difference can be seen as an aspect of the finding that the overlap of the many-body and mean-field wave functions can become much smaller than unity in the IPNL (Klaiman and Cederbaum, 2016). The variance of operators can thus be used to investigate the correlations in BECs that are ignored in mean-field models.

In turn, even at the IPNL the many-body wave function is extremely complex and very different from the mean-field one. This difference is caused by only a small amount of bosons outside the condensed mode (Cederbaum, 2017). Since the mean-field and many-body wave functions are different, the properties derived from them may also be different. This is particularly true starting from two-body properties, such as the many-particle position variance. When the variance is computed from a mean-field wave function it directly relates to the one-body density, because the wave function is built as a product of one single-particle state. When the variance, however, is computed from a many-body wave function it directly relates to the one-body and two-body densities, i.e., it contains information about correlations in the wave function that is not necessarily built as a product of one single-particle state. The relation between the density of a BEC and the correlations within a BEC can therefore be probed via the variance of operators. The variance can be used as a sensitive diagnostic tool for the excitations of BECs (Theisen and Streltsov, 2016; Beinke, Cederbaum, and Alon, 2018), for analyzing the impact of the range of interactions (Haldar and Alon, 2018, 2019), and for assessing convergence of numerical approaches like MCTDH-B (Cosme, Weiss, and Brand, 2016; Alon and Cederbaum, 2018), see Figs. 5(d)–5(f) for an example convergence test with the position and momentum space variance,

$$\frac{1}{N}\Delta^2_{\hat{x}}(t)$$

and

$$\frac{1}{N}\Delta^2_{\hat{p}}(t),$$

respectively, in quench dynamics of attractively interacting anharmonically trapped bosons.

The many-body features of the variance of operators in a BEC depend on the strength and sign of the interaction, the geometry of the trap, and the observable under investigation, e.g., the position, momentum, or angular momentum (Klaiman and Alon, 2015; Klaiman, Streltsov, and Alon,

2016; Sakmann and Schmiedmayer, 2018; Alon, 2019a). For bosonic systems in two-dimensional traps, additional possibilities open up for the variance. Explicitly, when computed at the many-body and mean-field levels of theory, the respective variances can exhibit different anisotropies (Klaiman *et al.*, 2018) or reflect the different effective dimensionality (Alon, 2019b) of the bosonic system under investigation.

IV. MCTDH-F AND ELECTRONS IN ATOMS AND MOLECULES

Here we discuss selected applications of MCTDH-F, in some cases with the incorporation of a complete active space or RAS scheme, to electron dynamics in atoms and molecules. Before discussing applications of MCTDH-F that contain a comparison with experiment in Sec. IV.B, we introduce the used observables in the following section.

A. Extraction of observables

Using (RAS-)MCTDH-F, photoionization cross sections have been calculated using the flux method (Jäckle and Meyer, 1996). The procedure, involving exterior complex scaling, was described in detail (Haxton, Lawler, and McCurdy, 2011) and applications were presented for beryllium and molecular hydrogen fluoride (Haxton, Lawler, and McCurdy, 2012).

The direct method is based on expressing the observables of interest in terms of the reduced one-body density [Eq. (25) for $p = 1$] (Omiste, Li, and Madsen, 2017; Madsen *et al.*, 2018). To obtain an expression for the photoelectron momentum distribution, the starting point can be the density in coordinate space. The photoelectron distribution can then be obtained by a suitable integral transformation. The density in coordinate space at position $\mathbf{r}$ is obtained as the expectation value $\rho(\mathbf{r};t) = \langle\Psi|\hat{\Psi}^\dagger(\mathbf{r})\hat{\Psi}(\mathbf{r})|\Psi\rangle$; cf. Eq. (30). In second quantization, using the orbitals [Eq. (3)] and matrix elements of the one-body density [Eq. (10)], we obtain the density [see also Eqs. (25) and (27)]:

$$\rho(\mathbf{r};t) = \sum_{kq}\rho_{kq}\Phi_k^*(\mathbf{r};t)\Phi_q(\mathbf{r};t). \tag{36}$$

To obtain the photoelectron distribution, a projection on an exact scattering state $\psi_{\mathbf{k}}(\mathbf{r})$ with momentum $\mathbf{k}$ should be performed. If this projection is restricted to a region of the simulation volume, beyond an ionization radius, where the effect of the potential from the remaining ion is small, the projection can be performed to plane waves; if the long-range Coulomb interaction is still important in that region, the projection may be done to Coulomb scattering waves (Madsen *et al.*, 2007; Omiste, Li, and Madsen, 2017). The photoelectron momentum distribution P is then [cf. Eq. (36)] given by

$$\frac{dP}{d\mathbf{k}} = \sum_{kq}\rho_{kq}\tilde{\Phi}_k^*(\mathbf{k};t)\tilde{\Phi}_q(\mathbf{k};t), \tag{37}$$

where

$$\tilde{\Phi}_j(\mathbf{k},t) = \int' d\mathbf{r}\psi_{\mathbf{k}}^*(\mathbf{r})\Phi_j(\mathbf{r};t), \tag{38}$$

and the prime on the integral sign denotes that the integral is only to be evaluated in the outer part of the simulation volume. From the momentum distribution, the energy distribution and the angular distribution can be obtained by integration. Recently, the time-dependent surface flux method (Tao and Scrinzi, 2012) was applied to argon and neon within a multiconfigurational framework (Orimo, Sato, and Ishikawa, 2019). This method is also based on Eqs. (37) and (38), but requires smaller simulation volumes. The cross section can be obtained from the time-dependent calculation once the ionization probability P_1 is known (Madsen, Nikolopoulos, and Lambropoulos, 2000; Foumouo *et al.*, 2006). For example, the photoionization cross section can be extracted by (Foumouo *et al.*, 2006)

$$\sigma_1(\mathrm{Mb}) = 1.032\times10^{14}\omega^2 P_1/n_p I_0, \tag{39}$$

where ω is the angular frequency of the laser, I_0 is the peak intensity of the laser pulse in $\mathrm{W/cm^2}$, n_p is the number of cycles, and P_1 is the ionization probability.

Another quantity which we use later and which has received significant interest in strong-field and attosecond physics in recent years is time delay in photoemission. This field was recently reviewed (Pazourek, Nagele, and Burgdörfer, 2015). The time delay τ can be extracted in a three-step procedure that we now discuss. (i) From the computed wave function, one extracts the expectation value of the radial distance $\langle r_{\vec{\xi}}(t)\rangle$ in a given direction $\vec{\xi}$ as a function of time and the linear momentum of the photoelectron, $k_{\vec{\xi}}$ in that direction; it can be evaluated in different ways. For instance $\langle k_{\vec{\xi}}\rangle$ can be evaluated via integrating only in the outer part of the simulation volume (Omiste, Li, and Madsen, 2017; Omiste and Madsen, 2018). (ii) Using $\langle r_{\vec{\xi}}(t)\rangle$ and $\langle k_{\vec{\xi}}\rangle$ the effective ionization time

$$t_{\mathrm{Coul}} = t - \frac{\langle r_{\vec{\xi}}(t)\rangle}{k_{\vec{\xi}}} = \tau_{\mathrm{EWS}} + \Delta t_{\mathrm{Coul}} \tag{40}$$

can be evaluated. Here τ_{EWS} is the Eisenbud-Wigner-Smith (EWS) time delay, i.e., the time delay without the interaction with the Coulomb tail of the ion and

$$\Delta t_{\mathrm{Coul}} = \frac{Z}{k_{\vec{\xi}}^3}[1 - \ln(2k_{\vec{\xi}}^2 t)]$$

is the distortion caused by the long-ranged Coulomb potential, where Z is the charge of the ion. (iii) Finally, the time delay is evaluated using

$$\tau = \tau_{\mathrm{EWS}} + \tau_{\mathrm{CLC}}. \tag{41}$$

Here τ_{EWS} can be evaluated from Eq. (40) and the Coulomb-laser coupling

$$\tau_{\mathrm{CLC}} = \frac{Z}{k_{\vec{\xi}}^3}\left[2 - \ln\left(\frac{\pi k_{\vec{\xi}}^2}{\omega_{\mathrm{IR}}}\right)\right]$$

which is known, because Z, $k_{\vec{\xi}}$, and the frequency of the infrared pulse ω_{IR} are known. Thus the time delay τ can readily

be extracted from the solution of the (RAS-)MCTDH-F EOMs (Omiste and Madsen, 2018).

B. Examples involving comparison with experimental results

The processes we focus on here are in the research area of laser-matter interactions. They are characterized by linear or perturbative interactions, where relatively few photons are exchanged with the external electromagnetic field. This reflects the current challenges with making the MCTDH-F computationally efficient in full dimension and for nonperturbative dynamics where many photons are exchanged. For validation of the MCTDH-F methodology, comparisons with experiments have focused on calculating photoabsorption cross sections (Haxton, Lawler, and McCurdy, 2012; Omiste and Madsen, 2018, 2019), where accurate experimental data are available. In addition, extreme ultraviolet (XUV) transient absorption spectra (Liao *et al.*, 2017) and time delays in photoionization dynamics (Omiste, Li, and Madsen, 2017; Omiste and Madsen, 2018) have been considered. Here we consider cross section and time-delay studies as illustrative examples.

1. Photoionization cross sections

In the case of photoionization, Fig. 6(a) shows a comparison for atomic neon between the predictions of theory at different levels of approximation and experimental cross section data.

The values of the theoretical cross sections in Fig. 6(a) are obtained by the procedure described in Sec. IV.A. From the agreement between theory and experiment in Fig. 6(a), it can be concluded that it is possible to obtain a precise prediction of the photoionization cross section using an explicitly time-dependent method, the RAS-MCTDH-F, using the procedure discussed in relation to Eq. (39). A second key point to be noticed from Fig. 6(a) is related to the choice of the $\mathcal{P}_1$ and $\mathcal{P}_2$ subspaces and the number of orbitals in them. We consider here the RAS-MCTDH-F-D method; cf. Fig. 2 for an illustration of the $\mathcal{P}_1$ and $\mathcal{P}_2$ spaces. The "D" in the acronym of the method denotes "doubles": only double excitations from the $\mathcal{P}_1$ to the $\mathcal{P}_2$ spaces are allowed. In this example there is no space $\mathcal{P}_0$ with always occupied orbitals like the one used to construct "complete active space" methods (Sato and Ishikawa, 2013). Such a choice of active space and excitation scheme reduces the number of configurations compared with the MCTDH-F method with no restrictions, and as seen from Fig. 6(a), can still yield accurate results: convergence is obtained by increasing the number of orbitals in $\mathcal{P}_2$ from $M_2 = 0$ to 9. In this manner the accuracy of different approximations from the mean-field TDHF method to approaches including more correlations is systematically explored.

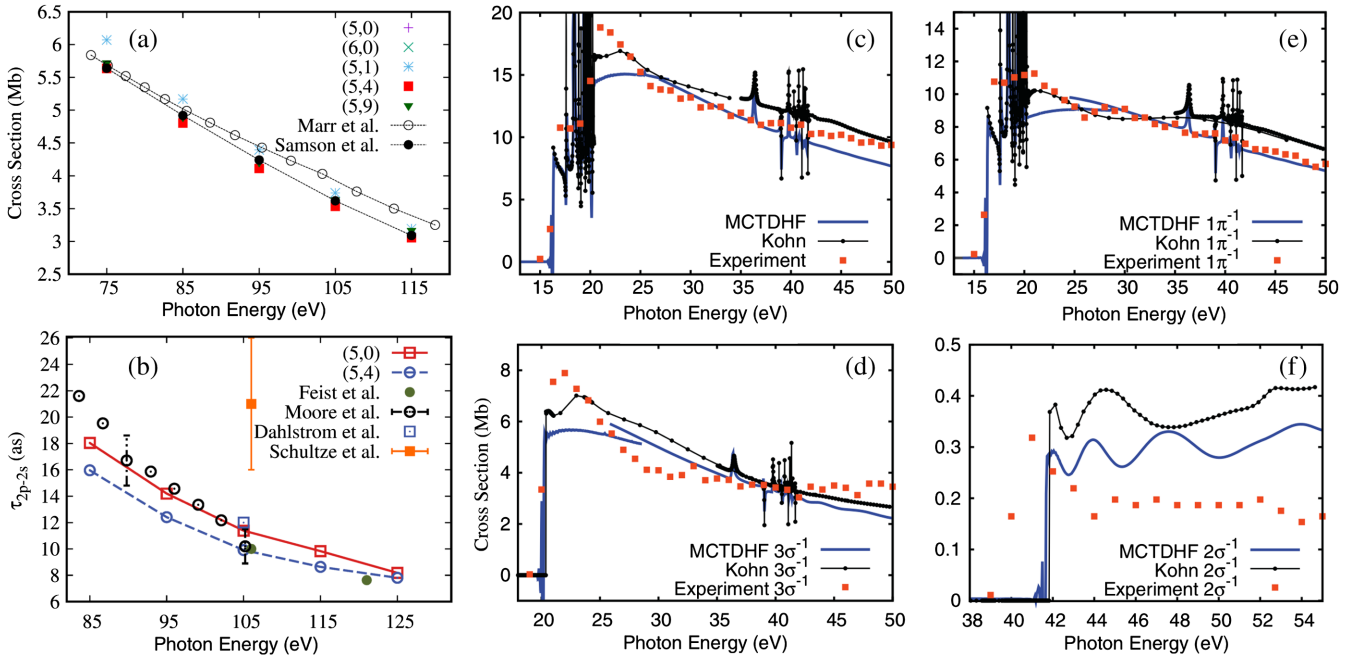

FIG. 6. (a) Theoretical total photoionization cross section extracted from a calculation with a 10-cycle linearly polarized pulse with peak intensity 10^{14} W/cm^2 as a function of the central angular frequency ω of the laser for several RAS schemes compared to the experimental data by Marr and West (1976) and Samson and Stolte (2002). (b) Relative time delay of ionization in Ne, τ_{2p-2s}, as a function of the central frequency of the XUV pulse for a 780 nm IR pulse for $(M_1, M_2) = (5, 0)$ and (5,4) together with calculations (Moore *et al.*, 2011; Dahlström, Carette, and Lindroth, 2012; Feist *et al.*, 2014) and the measurement (Schultze *et al.*, 2010). (c) Total photoionization cross section and its partitions in the (e) $1\pi^{-1}$, (d) $3\sigma^{-1}$, and (f) $2\sigma^{-1}$ final states. The MCTDH-F computations here used nine orbitals while the complex Kohn ones used eight. The cross sections were computed via the flux into an exterior complex scaling region (Moiseyev, 1998); see Haxton, Lawler, and McCurdy (2012) for details. The overall agreement between MCTDH-F and experimental results (Brion and Thomson, 1984) is good: for all four depicted cases the salient features are reproduced for the total, $1\pi^{-1}$, and $3\sigma^{-1}$ cross sections. From Omiste and Madsen, 2018, and Haxton, Lawler, and McCurdy, 2012.

Comparisons between theory and experiment for photoionization cross sections have also been performed for atomic beryllium and the hydrogen fluoride molecule (Haxton, Lawler, and McCurdy, 2012). In these latter cases, full MCTDH-F is considered. Similar to the RAS-MCTDH-F example, convergence of the MCTDH-F results for the cross sections were obtained with an increasing number of active orbitals. We highlight here the good agreement of the photoionization cross sections obtained for hydrogen fluoride molecules with the experimental (Brion and Thomson, 1984) and complex Kohn theoretical (Schneider and Rescigno, 1988; Rescigno and Orel, 1991) results; see Figs. 6(c)–6(f).

2. Time delay in photoionization

RAS-MCTDH-F was applied to the time delay in photoionization in neon (Omiste and Madsen, 2018), where experimental data are available (Schultze *et al.*, 2010; Isinger *et al.*, 2017). It is the advent of new light sources for ultrashort light pulses with durations down to the attosecond timescale that has allowed addressing questions like time delay in photoionization in experiments. In Fig. 6(b), the time delay in photoionization between the $2s$ and the $2p$ electrons in neon is shown in units of attoseconds (1 as $= 10^{-18}$ s). A collection of theoretical results and a measurement point (Schultze *et al.*, 2010) are presented in Fig. 6(b) as a function of photon energy ω (in atomic units, $\hbar = 1$, and for convenience the values in atomic units have been converted to eV, 1 a.u. $= 27.21$ eV).

The positive value of the time delay can be interpreted as if it takes a longer time for the $2p$ than for the $2s$ orbital to ionize. Such an interpretation in terms of orbitals, however, assumes a mean-field picture. Theory and experiment have addressed the question about relative time delay between ionization into the two channels

$$\mathrm{Ne}[(1s^2 2s^2 2p^6)^1 S^e] \rightarrow \mathrm{Ne}^+[(1s^2 2s^2 2p^5)^2 P^o] + e^-(s,d),$$

$$\mathrm{Ne}[(1s^2 2s^2 2p^6)^1 S^e] \rightarrow \mathrm{Ne}^+[(1s^2 2s 2p^6)^2 S^e] + e^-(p), \quad (42)$$

where the dominant configurations have been used to denote the ground state in the neutral as well as the ground and excited states in the ion. Note that dipole selection rules dictate the possible values of the angular momenta in the final channels. From Fig. 6(b), it is seen that all the theories predict a decreasing time delay as a function of the photon energy in the considered energy range. All theoretical values are also smaller than the experimental result. Recently, measurements with an interferometric technique (Isinger *et al.*, 2017) reported a lower value of the time delay in better agreement with the theory results. In the following, we focus on the RAS-MCTDH-F results with (M_1, M_2) at (5,0) and (5,4); see Fig. 6(b). For neon, the (5,0) results correspond to the TDHF case, i.e., one active orbital for each pair of electrons. The (5,4) case includes more correlation and has five orbitals in $\mathcal{P}_1$ and four orbitals in $\mathcal{P}_2$. The transitions between $\mathcal{P}_1$ and $\mathcal{P}_2$ occur by double excitation only. As seen from Fig. 6(b), part of the overall trend of the time delay can be described at the TDHF level of theory.

Note that there are other cases of interest, where the ionization step cannot be captured by TDHF. For example, in beryllium, photoionization of the ground state into the channel $\mathrm{Be}^+[(1s^2 2p)^2 \mathrm{P}^o] + e^-(s \text{ or } d)$ changes two orbitals in the dominant configurations by the action of the one-body photoionization operator. Therefore, that process cannot be described by TDHF (Omiste, Li, and Madsen, 2017).

V. APPLICATIONS, THEORETICAL, AND NUMERICAL DEVELOPMENT

We now discuss theoretical and numerical developments within and beyond (RAS-)MCTDH-X.

A. MCTDH-X-based development

1. Numerical methods

Since the introduction of MCTDH-F (Zanghellini *et al.*, 2003; Kato and Kono, 2004; Caillat *et al.*, 2005) and MCTDH-B (Alon, Streltsov, and Cederbaum, 2007c, 2008; Streltsov, Alon, and Cederbaum, 2007b) many numerical techniques and theory extensions were developed that extend the applicability of MCTDH-X.

For long-ranged interparticle interactions where the interaction potential is a function of the distance of the particles $W(\mathbf{r}_i, \mathbf{r}_j; t) = W(\mathbf{r}_i - \mathbf{r}_j; t)$, the so-called interaction matrix evaluation via successive transforms (IMEST) has been developed (Sakmann, 2011). IMEST rewrites the local interaction potentials as a collocation using fast Fourier transforms. IMEST has been applied for solving the TDSE with MCTDH-X, for time-dependent harmonic interparticle interactions (Lode, Sakmann *et al.*, 2012; Lode, 2015; Fasshauer and Lode, 2016), dipolar interactions (Chatterjee and Lode, 2018; Chatterjee *et al.*, 2019; Chatterjee, Tsatsos, and Lode, 2019), and general long-range interaction potentials (Streltsov, 2013; Streltsova *et al.*, 2014; Fischer, Lode, and Chatterjee, 2015; Haldar and Alon, 2018) and screened Coulomb interactions (Fasshauer and Lode, 2016).

The development of an implementation of MCTDH-F using a multiresolution Cartesian grid (Sawada, Sato, and Ishikawa, 2016) holds promise to provide improved adaptive representations for the dynamics of the wave function of electrons in atoms and molecules. Moreover, we note the implementation of the infinite-range exterior complex scaling method (Orimo *et al.*, 2018) and the introduction of a space partitioning concept (Miyagi and Madsen, 2017) in combination with RAS-MCTDH-F. We mention that it has been shown that the inclusion of complex absorbing potentials to describe situations like ionization where particles are leaving the region of interest requires one to use a master equation of Lindblad form for the time evolution of the density matrix (Selstø and Kvaal, 2010). To solve this master equation, ρ-MCTDH-F was formulated by Kvaal (2011).

The efficient evaluation of the Coulomb interaction integrals [Eq. (16) with $\hat{W}$ being the Coulomb interaction] is instrumental to study real-world dynamics of electrons in atoms and molecules in three spatial dimensions. We mention here a discrete variable representation using sin$c$ functions

that enables an efficient collocation, i.e., fast-Fourier-transform-based evaluation of the Coulomb interactions by exploiting the triple-Toeplitz structure of the kinetic energy operator (Jones *et al.*, 2016).

We note the recent successful implementation and application of the adaptive removal and addition of configurations, the so-called *dynamical pruning* (Larsson and Tannor, 2017; Wodraszka and Carrington, 2017) for dynamics computed with MCTDH-B (Köhler *et al.*, 2019).

2. Theoretical progress

The MCTDH-X methodology has also been used to obtain descriptions of the dynamics generated by Hubbard Hamiltonians. Lode and Bruder (2016) expressed the operators that create or annihilate particles in the time-independent first-band Wannier basis functions of the Hubbard lattice as effective, creation or annihilation operators that create particles in a time-dependent superposition of all lattice sites. The resulting EOMs are identical to the MCTDH-X EOMs [Eqs. (8) and (13)], albeit with a special representation of the kinetic and potential energy. Sakmann *et al.* (2011) proposed generalized time-dependent Wannier functions which are a superposition of many bands to increase the accuracy of the representation of the many-boson wave function beyond the single-band Hubbard model. Grond *et al.* (2013) and Alon, Streltsov, and Cederbaum (2014) derived a linear-response framework for the EOMs of MCTDH-X, the so-called LR-MCTDH-X, that allows one to obtain highly accurate information about the excitation spectrum of the considered many-body Hamiltonian as benchmarked by Beinke *et al.* (2017) and Beinke, Cederbaum, and Alon (2018). Recently, the Fourier transform of the autocorrelation function was used to also obtain the spectrum for a bosonic many-body system (Lévêque and Madsen, 2019; Roy *et al.*, 2019).

For the dynamics of electrons in molecules, an approach termed the "multiconfiguration electron-nuclear dynamics method" (MCEND) was developed (Nest, 2009) and applied to lithium hydride (Ulusoy and Nest, 2012). This MCEND method represents the total molecular wave function as a direct (tensor) product of an MCTDH-type wave function for the nuclei with an MCTDH-F-type wave function of the electrons. Other approaches to deal with coupled electronic and nuclear dynamics have been developed and applied for diatomics (Kato and Yamanouchi, 2009; Haxton, Lawler, and McCurdy, 2011, 2015; Lötstedt, Kato, and Yamanouchi, 2019b).

Developments of the so-called extended-MCTDH-F by Kato and Yamanouchi (2009) considered coupled electron-nuclear dynamics and molecular wave functions and include extensive investigations on molecular hydrogen (Ide, Kato, and Yamanouchi, 2014; Kato, Ide, and Yamanouchi, 2015) and cationic molecular hydrogen in intense laser fields (Lötstedt, Kato, and Yamanouchi, 2019a, 2019b) as well as a strategy to efficiently partition the configuration space of MCTDH-F (Lötstedt, Kato, and Yamanouchi, 2016).

The multiple active space model put forward by Sato and Ishikawa (2015) introduced a flexible and possibly adaptive approach to construct representations for the N-body Hilbert space with multiconfigurational methods.

We mention here the development, application, and successful benchmark against MCTDH-F predictions for high-harmonic generation of a method that time evolves the two-body density matrix [cf. Eq. (25) for $p = 2$] without resorting to a wave function at all (Lackner *et al.*, 2015, 2017). These methods for the two-body density matrix offer a similar accuracy to MCTDH-F approaches while being much less computationally demanding.

The unfavorable scaling of the number of coefficients in the MCTDH-X *Ansatz* with the number of orbitals impedes the application of MCTDH-X to systems with many electrons or many bosons with more than a few orbitals. Truncation strategies for the coefficient vector include the RAS approach from quantum chemistry (Olsen *et al.*, 1988) that results in RAS-MCTDH-F (Miyagi and Madsen, 2013, 2014b) and RAS-MCTDH-B (Lévêque and Madsen, 2017, 2018) theories including a special consideration of single-particle excitations (Miyagi and Madsen, 2014a). The "complete active space" truncation approach to limit the number of coefficients was also investigated (Sato and Ishikawa, 2013), including a generalization to several active spaces (Sato and Ishikawa, 2015). For an MCTDH-F formulation for completely general configuration spaces where different variational principles become inequivalent, see Haxton and McCurdy (2015).

For a review of time-dependent multiconfigurational theories for electronic and nuclear motion in molecules in intense fields, see Kato, Yamanouchi, and Kono (2018). For an overview of RAS-MCTDH-X theory, see Madsen *et al.* (2018).

B. MCTDH-B applications

The archetypical example for the emergence of fragmentation in systems of interacting bosons is the double-well potential (Spekkens and Sipe, 1999). Using MCTDH-B for bosons in double-well traps, the reduced density matrices and Glauber correlation functions (Sakmann *et al.*, 2008), the dynamical emergence (Streltsov, Alon, and Cederbaum, 2007b; Sakmann *et al.*, 2009, 2010; Sakmann, 2011), and the universality (Sakmann *et al.*, 2014) of fragmentation have been investigated. It is worthwhile to highlight that the works (Sakmann *et al.*, 2009, 2010) report converged solutions of the TDSE and demonstrate that the commonly applied Bose-Hubbard model may fail to describe the many-body states for parameter regimes where it was deemed to yield a good approximation to the many-body state. We note that the excitation spectra of interacting bosons in double wells (Grond *et al.*, 2013; Theisen and Streltsov, 2016), in lattices (Beinke *et al.*, 2017), and under rotation (Beinke, Cederbaum, and Alon, 2018) have been investigated with LR-MCTDH-B. Recent work with MCTDH-B explores the connection between quantum fluctuations, correlations, and fragmentation (Marchukov and Fischer, 2019; Nguyen *et al.*, 2019).

Solitons in BECs are thought to be coherent and condensed; several investigations with MCTDH-B (Streltsov, Alon, and Cederbaum, 2008, 2011; Cosme, Weiss, and Brand, 2016), however, have shown that fragmentation and correlations do emerge in their dynamics.

Vortices in ultracold bosonic atoms are conventionally modeled by mean-field approaches (Gross, 1961; Pitaevskii,

1961). Applications of MCTDH-B to interacting bosonic atoms have, however, demonstrated that correlations and fragmentation may emerge as soon as the many-body state contains significant angular momentum (Beinke *et al.*, 2015; Tsatsos and Lode, 2015; Weiner *et al.*, 2017). This emergence of correlations and fragmentation marks the breakdown of the mean-field description and is anticipated from pronounced many-body effects in the excitation spectra of bosonic systems with angular momentum as obtained from LR-MCTDH-B (Beinke, Cederbaum, and Alon, 2018).

BECs in high-finesse optical cavities have been used as a quantum simulator for the Dicke model (Brennecke *et al.*, 2007; Baumann *et al.*, 2010). Using MCTDH-B it was shown that the phase diagram of the cold-atom system in the cavity is richer than the phase diagram of the Dicke model and thus the mapping to the Dicke model may break down (Lode and Bruder, 2017; Lode *et al.*, 2018; Lin *et al.*, 2019).

C. MCTDH-F applications

The MCTDH-F was first applied to strong-field ionization of one-dimensional (1D) model molecules with up to eight electrons (Zanghellini *et al.*, 2003), harmonic quantum dots, a 1D model of helium (Zanghellini *et al.*, 2004), and a 1D jellium model (Nest, Padmanaban, and Saalfrank, 2007). Total ionization spectra in strong laser fields were reported for 1D systems with up to six active electrons, and strong correlation effects were reported in the shape of photoelectron peaks and the dependence of ionization on molecule size (Caillat *et al.*, 2005). Later, the effect of the reduction in dimensionality from three to one dimension was discussed (Jordan *et al.*, 2006). In the strong-field regime, multielectron and polarization effects have been considered in connection with applications to high-order harmonic generation at a fixed internuclear distance in model systems (Jordan and Scrinzi, 2008; Sukiasyan *et al.*, 2009, 2010; Miyagi and Madsen, 2013, 2014b), in carbon monoxide (Ohmura *et al.*, 2018), as well as in helium, beryllium, and neon (Sawada, Sato, and Ishikawa, 2016).

In molecules, MCTDH-F was applied to molecular hydrogen at fixed internuclear distance (Kato and Kono, 2004, 2008). The MCTDH-F results reported for molecules include calculations of vertical excitation energies, transition dipole moments, and oscillator strengths for lithium hydride and methane (Nest, Padmanaban, and Saalfrank, 2007), as well as considerations of the response of lithium hydride to few-cycle intense pump fields followed by a probe pulse (Nest, Remacle, and Levine, 2008). Work on characterizing multielectron dynamics by considering energies and amplitudes was reported (Ohmura *et al.*, 2014). The inclusion of nuclear motion was also considered (Kato and Yamanouchi, 2009; Nest, 2009; Haxton, Lawler, and McCurdy, 2011; Anzaki, Sato, and Ishikawa, 2017).

Concerning few-photon processes, MCTDH-F was applied to the simulation of the two-photon ionization of helium including a comparison with the time-dependent configuration interaction method (Hochstuhl and Bonitz, 2011). The population transfer between two valence states of the lithium atom with a Raman process via intermediate autoionizing states well above the ionization threshold was investigated (Li, McCurdy, and Haxton, 2014). A two-color core-hole stimulated Raman process was studied in nitric oxide (Haxton and McCurdy, 2014) and Raman excitations of atoms through continuum levels were considered for neon (Greenman *et al.*, 2017). Moreover, a procedure was suggested for using transient absorption spectroscopy above the ionization threshold to measure the polarization of the continuum induced by an intense optical pulse (Li *et al.*, 2016). Recently, a comparison of MCTDH-F and experimental results was reported in a study using XUV transient absorption spectroscopy to study autoionizing Rydberg states of oxygen (Liao *et al.*, 2017). RAS-MCTDH-F was applied to study electron correlation and time delay in beryllium (Omiste, Li, and Madsen, 2017), neon (Omiste and Madsen, 2018), and effects of performing calculations with or without a filled core space (Omiste and Madsen, 2019).

D. Multilayer and second-quantized-representation approaches

Multilayer approaches (Wang and Thoss, 2003; Manthe, 2008) provide a powerful and promising generalization of the standard MCTDH. In the ML strategy, the MCTDH was applied recursively (Manthe, 2008; Vendrell and Meyer, 2011): first, the wave function is represented as a sum of products of "single-particle" functions (first layer); second, the single-particle functions of the first layer are again represented by an MCTDH-type wave function, i.e., a sum of products of second-layer single-particle functions, and so on. Here we used quotation marks on the term single particle, because several degrees of freedom may be combined into multimode single-particle functions using a mode combination (Worth, Meyer, and Cederbaum, 1998, 1999; Raab and Meyer, 2000), i.e., a single-particle function may still be a high-dimensional function. In the bottom or last layer, the single-particle functions are then expanded on a primitive time-independent basis.

We mention here a fundamental relation between the density matrix renormalization group and matrix-product-state methods reviewed by Schollwöck (2005, 2011) and ML-MCTDH: mathematically, both methods fall into the class of so-called hierarchical low-rank tensor approximations, a concept which has, for instance, enabled progress in devising new efficient time-integration schemes (Lubich, Vandereycken, and Walach, 2018; Falcó, Hackbusch, and Nouy, 2019) that are also applicable for (RAS-)MCTDH-X.

The multilayer approach requires a configuration space of *distinguishable* degrees of freedom as in MCTDH; the multilayer approach can thus not be directly combined with the MCTDH-X, since the latter restricts the configuration space to include only configurations of a fixed number of strictly *indistinguishable* particles that have the correct fermionic or bosonic symmetry.

In the following, we introduce two distinct multilayer approaches for indistinguishable particles, namely, the ML-MCTDH in second-quantized representation (ML-MCTDH-SQR) and the ML-MCTDH-X. ML-MCTDH-X and ML-MCTDH-SQR are not affected by the previous incompatibility of the MCTDH-X approach and multilayering. The ML-MCTDH-X approach uses a multilayer formalism for Cartesian coordinates or different species of indistinguishable particles and ML-MCTDH-SQR uses the occupation numbers

of the orbitals as distinguishable degrees of freedom for an MCTDH-type wave function where multilayering can be applied.

1. ML-MCTDH in second-quantized representation

We begin by noting that the SQR approach is actually independent of the ML approach. However, historically, SQR was introduced on top of ML-MCTDH; the resulting ML-MCTDH-SQR was derived by Wang and Thoss (2009) and reviewed by Wang (2015) and Manthe (2017). Next we discuss the two ingredients together.

The SQR approach is based on the fact that all the second-quantized configurations $|\vec{n}\rangle = |n_1, ..., n_M\rangle$ used in Eq. (2) can formally be written as a Hartree product (Röpke, 1999):

$$|n_1, n_2, \ldots, n_M\rangle \equiv |n_1\rangle|n_2\rangle \cdots |n_M\rangle. \tag{43}$$

Thus, the occupation numbers $n_1, n_2, \ldots, n_M$ of the time-independent orbitals are used as the degrees of freedom in an ML-MCTDH-type wave function to obtain the *Ansatz* of the ML-MCTDH-SQR approach.

Just like ML-MCTDH, the ML-MCTDH-SQR representation features a configurational expansion of distinguishable degrees of freedom; however, these degrees of freedom are, unlike for standard ML-MCTDH, represented in a second-quantized notation tied to a time-independent basis. As Eq. (43) demonstrates, the ML-MCTDH-SQR breaks apart the configurations $|n_1, \ldots, n_M\rangle$, whereas the (ML-)MCTDH-X approach deals with them as unbreakable entities. ML-MCTDH-SQR therefore, via employing a different approach to the representation of Fock space, uses multilayering in the very same way as the original ML-MCTDH, but now for indistinguishable particles. In other words, ML-MCTDH-SQR thus enables the use of deeply multilayered wave-function representations which is incompatible with the particle-number-based configuration selection of the MCTDH-X approaches. We note that the reformulation of a configuration as a Hartree product in Eq. (43) requires that, for the case of indistinguishable fermions, the initially chosen order of the terms in the product has to be tracked and maintained at all times (Wang and Thoss, 2009; Wang, 2015).

The ML-MCTDH-SQR theory has, for instance, been successfully applied to the dynamics of vibrationally coupled electron transport in a model molecular junction (Wang and Thoss, 2009, 2016) and transport in the Anderson impurity model (Wang and Thoss, 2018). Recently, ML-MCTDH-SQR was generalized to allow for variationally time-dependent optimized second-quantized (oSQR) degrees of freedom yielding the ML-MCTDH-oSQR approach (Manthe and Weike, 2017). Most recently, strategies to incorporate particle conservation in ML-MCTDH-oSQR were discussed by Weike and Manthe (2020).

2. ML-MCTDH-X

The ML-MCTDH-X approach uses an MCTDH-type representation for the distinguishable degrees of freedom in systems of identical particles. These distinguishable degrees of freedom can be the species in a mixture of identical particles, the differernt Cartesian coordinates of an orbital in more than one spatial dimension, and/or its spin. The indistinguishable parts of the wave function in ML-MCTDH-X are, themselves, represented by MCTDH-X-type expansions (Cao *et al.*, 2013, 2017; Krönke *et al.*, 2013). In other words, in ML-MCTDH-X the statistics of indistinguishable particles is maintained via an MCTDH-X-type wave function. We note that an MCTDH-X formulation for mixtures of identical particles without multilayering exists (Alon, Streltsov, and Cederbaum, 2007a). The ML-MCTDH-X approach was applied successfully to mixtures of ultracold bosons and fermions (Erdmann, Mistakidis, and Schmelcher, 2018; Mistakidis *et al.*, 2018; Siegl, Mistakidis, and Schmelcher, 2018) and bosons in more than one spatial dimension (Bolsinger, Krönke, and Schmelcher, 2017a, 2017b).

E. Orbital-adaptive time-dependent coupled cluster

To reduce the numerical effort in solving the TDSE to become polynomial, the so-called coupled-cluster method (CC) (Coester and Kümmel, 1960; Čížek, 1966, 2007; Čížek and Paldus, 1971) can be employed. Although CC uses a different type of *Ansatz* than MCTDH-X, we mention it here because recent developments include approaches with a time-dependent, variationally optimized basis and are thus related to MCTDH-X and RAS-MCTDH-X.

The conventional (time-dependent) CC uses time-dependent excitation amplitudes, but does not use a set of time-dependent orbitals in the representation of the wave function. The standard CC's *Ansatz* can be generalized to include time-dependent amplitudes and orbitals. This generalization of the *Ansatz* in combination with a generalized, so-called bivariational principle leads to the equations of motion of the orbital-adapted time-dependent coupled-cluster theory (Kvaal, 2012, 2013; Pedersen and Kvaal, 2019). We identify the application of the bivariational principle for the derivation of the MCTDH-X EOMs for *Ansätze* with restricted configuration spaces [as in Eq. (17)] as an open question.

When a real-valued variational principle is used, the fully time-dependent coupled-cluster *Ansatz* yields the EOMs of the time-dependent optimized CC (Sato *et al.*, 2018a, 2018b). The latter theory allows the self-consistent computation of eigenstates via imaginary time propagation and has been applied to single and double ionization as well as high-harmonic generation in argon (Sato *et al.*, 2018a).

VI. CONCLUSIONS AND FRONTIERS

In this Colloquium, we introduced the MCTDH-B and MCTDH-F methods for full and restricted configuration spaces. We highlighted the use and versatility of MCTDH-X with benchmarks against exactly solvable models as well as direct comparisons with experimental applications.

The development of methods for the time-dependent many-body Schrödinger equation in the field of MCTDH-X and beyond, that we portrayed in this Colloquium, has yielded highly efficient and flexible numerical approaches. This flexibility, however, comes with an increasing number of parameters to tune the performance and accuracy of the

given approach; examples include the tree structure in multilayering approaches (Wang and Thoss, 2009; Manthe, 2015; Wang, 2015; Manthe and Weike, 2017), and the partitioning of Hilbert space into multiple occupation-restricted active spaces (Sato and Ishikawa, 2015) or $\mathcal{P}_1$ and $\mathcal{P}_2$ (Fig. 2) in the RAS-MCTDH-X approach (Miyagi and Madsen, 2013, 2014b; Lévêque and Madsen, 2017, 2018). We thus observe that the recent methodological developments demand an ever larger and more complicated set of parameters to be configured by their users.

Such a development toward higher complexity in the application of methods is not desirable, because it makes applications ever more tedious. The trend toward more complexity could possibly be overcome by introducing additional adaptivity. We mention here the recent developments with adaptive tensor representations (Grasedyck, Kressner, and Tobler, 2013; Ballani and Grasedyck, 2014), an adaptive number of configurations (Miyagi and Madsen, 2013, 2014b; Haxton and McCurdy, 2015; Larsson and Tannor, 2017; Lévêque and Madsen, 2017; Wodraszka and Carrington, 2017; Köhler *et al.*, 2019), an adaptive number of single-particle functions (Lee and Fischer, 2014; Mendive-Tapia *et al.*, 2017), optimally chosen unoccupied orbitals (Manthe, 2015), adaptive grids (Sawada, Sato, and Ishikawa, 2016), and an adaptive construction of the many-particle Hilbert space (Sato and Ishikawa, 2015). We thus envision a flexible theory and implementation that combines multiple of these multiconfigurational methods in an adaptive framework to solve the many-particle Schrödinger equation: according to a simple or single input, for instance an error threshold, the Hilbert space is automatically and adaptively partitioned while for each of its partitions the most suitable multiconfigurational method (or an adaptive version of which) is to be used.

Interestingly, the extended-MCTDH-F and MCEND *Ansätze*, proposed by Kato and Yamanouchi (2009) and Nest (2009), respectively, represent the total wave function as a tensor product of wave functions of different species of particles. In the case of extended-MCTDH-F, the wave function is a product of two MCTDH-F-type wave functions and in the case of MCEND, the wave function is a product of an MCTDH-F-type wave function with an MCTDH-type wave function for distinguishable particles. Such a multispecies wave function, as well as bulk of the multiconfigurational methods developed for restricted, multiple, and general active spaces, is amenable to multilayer approaches. The combination of truncation methods for the configuration space, including the dynamical pruning approaches (Larsson and Tannor, 2017; Wodraszka and Carrington, 2017; Köhler *et al.*, 2019), with ML-MCTDH-X or ML-MCTDH-(o)SQR is one of the frontiers that we see in the further development with multiconfigurational approaches.

LIST OF SYMBOLS AND ABBREVIATIONS

BEC	Bose-Einstein condensate
EOMs	equations of motion
IPNL	infinite particle number limit
MCTDH	multiconfigurational time-dependent Hartree (approach)
MCTDH-B	MCTDH for bosons
MCTDH-F	MCTDH for fermions
MCTDH-X	MCTDH for indistinguishable particles X
ML	multilayer
RAS	restricted active space
RDM	reduced density matrix
(o)SQR	(optimized) second-quantized representation
TDHF	time-dependent Hartree-Fock (method)
(TD-)HIM	(time-dependent) harmonic interaction model
TDSE	time-dependent many-body Schrödinger equation

ACKNOWLEDGMENTS

Financial support by the Austrian Science Foundation (FWF) under Grants No. P-32033 and No. M-2653, the Wiener Wissenschafts-und TechnologieFonds (WWTF) Grant No. MA16-066, the Israel Science Foundation (Grants No. 600/15 and No. 1516/19), and the Villum Kann Rasmussen (VKR) Center of Excellence, QUSCOPE, Quantum Scale Optical Processes, and computation time on the HazelHen Cray computer at the HLRS Stuttgart is gratefully acknowledged.

REFERENCES

Alon, O. E., 2019a, Symmetry **11**, 1344.
Alon, O. E., 2019b, Mol. Phys. **117**, 2108.
Alon, O. E., and L. S. Cederbaum, 2018, Chem. Phys. **515**, 287.
Alon, O. E., A. I. Streltsov, and L. S. Cederbaum, 2007a, Phys. Rev. A **76**, 062501.
Alon, O. E., A. I. Streltsov, and L. S. Cederbaum, 2007b, Phys. Lett. A **362**, 453.
Alon, O. E., A. I. Streltsov, and L. S. Cederbaum, 2007c, J. Chem. Phys. **127**, 154103.
Alon, O. E., A. I. Streltsov, and L. S. Cederbaum, 2008, Phys. Rev. A **77**, 033613.
Alon, O. E., A. I. Streltsov, and L. S. Cederbaum, 2014, J. Chem. Phys. **140**, 034108.
Anzaki, R., T. Sato, and K. L. Ishikawa, 2017, Phys. Chem. Chem. Phys. **19**, 22008.
Armstrong, J. R., N. T. Zinner, D. V. Fedorov, and A. S. Jensen, 2011, J. Phys. B **44**, 055303.
Ballani, J., and L. Grasedyck, 2014, SIAM J. Sci. Comput. **36**, A1415.
Bassaganya-Riera, J., and R. Hontecillas, 2015, *Introduction to Computational Immunology* (Wiley, New York).
Baumann, K., C. Guerlin, F. Brennecke, and T. Esslinger, 2010, Nature (London) **464**, 1301.
Beck, M. H., A. Jäckle, G. A. Worth, and H. D. Meyer, 2000, Phys. Rep. **324**, 1.
Beinke, R., L. S. Cederbaum, and O. E. Alon, 2018, Phys. Rev. A **98**, 053634.
Beinke, R., S. Klaiman, L. S. Cederbaum, A. I. Streltsov, and O. E. Alon, 2015, Phys. Rev. A **92**, 043627.

Beinke, R., S. Klaiman, L. S. Cederbaum, A. I. Streltsov, and O. E. Alon, 2017, Phys. Rev. A **95**, 063602.

Bolsinger, V. J., S. Krönke, and P. Schmelcher, 2017a, J. Phys. B **50**, 034003.

Bolsinger, V. J., S. Krönke, and P. Schmelcher, 2017b, Phys. Rev. A **96**, 013618.

Brennecke, F., T. Donner, S. Ritter, T. Bourdel, M. Köhl, and T. Esslinger, 2007, Nature (London) **450**, 268.

Brion, C. E., and J. P. Thomson, 1984, J. Electron Spectrosc. Relat. Phenom. **33**, 301.

Burger, S., K. Bongs, S. Dettmer, W. Ertmer, and K. Sengstock, 1999, Phys. Rev. Lett. **83**, 5198.

Caillat, J., J. Zanghellini, M. Kitzler, O. Koch, W. Kreuzer, and A. Scrinzi, 2005, Phys. Rev. A **71**, 012712.

Calogero, F., 1969, J. Math. Phys. (N.Y.) **10**, 2191.

Calogero, F., and A. Degasperis, 1975, Phys. Rev. A **11**, 265.

Cao, L., V. Bolsinger, S. I. Mistakidis, G. M. Koutentakis, S. Krönke, J. M. Schurer, and P. Schmelcher, 2017, J. Chem. Phys. **147**, 044106.

Cao, L., S. Krönke, O. Vendrell, and P. Schmelcher, 2013, J. Chem. Phys. **139**, 134103.

Castin, Y., and J. Dalibard, 1997, Phys. Rev. A **55**, 4330.

Castin, Y., and R. Dum, 1998, Phys. Rev. A **57**, 3008.

Cederbaum, L. S., 2017, Phys. Rev. A **96**, 013615.

Chatterjee, B., and A. U. J. Lode, 2018, Phys. Rev. A **98**, 053624.

Chatterjee, B., J. Schmiedmayer, C. Lévêque, and A. U. J. Lode, 2019, arxiv:1904.03966.

Chatterjee, B., M. C. Tsatsos, and A. U. J. Lode, 2019, New J. Phys. **21**, 033030.

Čižek, J., and J. Paldus, 1971, Int. J. Quantum Chem. **5**, 359.

Čížek, J., 1966, J. Chem. Phys. **45**, 4256.

Čížek, J., 2007, Adv. Chem. Phys. **14**, 35.

Coester, F., and H. Kümmel, 1960, Nucl. Phys. **17**, 477.

Cohen, L., and C. Lee, 1985, J. Math. Phys. (N.Y.) **26**, 3105.

Cosme, J. G., C. Weiss, and J. Brand, 2016, Phys. Rev. A **94**, 043603.

Dahlström, J. M., T. Carette, and E. Lindroth, 2012, Phys. Rev. A **86**, 061402.

Dirac, P. A. M., 1927, Proc. R. Soc. A **114**, 243.

Dirac, P. A. M., 1930, Math. Proc. Cambridge Philos. Soc. **26**, 376.

Dukelsky, J., and P. Schuck, 2001, Phys. Rev. Lett. **86**, 4207.

Dziarmaga, J., Z. P. Karkuszewski, and K. Sacha, 2003, J. Phys. B **36**, 1217.

Edwards, M., and K. Burnett, 1995, Phys. Rev. A **51**, 1382.

Engels, P., C. Atherton, and M. A. Hoefer, 2007, Phys. Rev. Lett. **98**, 095301.

Erdmann, J., S. I. Mistakidis, and P. Schmelcher, 2018, Phys. Rev. A **98**, 053614.

Erdős, L., B. Schlein, and H.-T. Yau, 2007a, Phys. Rev. Lett. **98**, 040404.

Erdős, L., B. Schlein, and H.-T. Yau, 2007b, Invent. Math. **167**, 515.

Falcó, A., W. Hackbusch, and A. Nouy, 2019, Found. Comput. Math. **19**, 159.

Faraday, M., 1830, Proc. R. Soc. London **3**, 49.

Fasshauer, E., and A. U. J. Lode, 2016, Phys. Rev. A **93**, 033635.

Feist, J., O. Zatsarinny, S. Nagele, R. Pazourek, J. Burgdörfer, X. Guan, K. Bartschat, and B. I. Schneider, 2014, Phys. Rev. A **89**, 033417.

Fischer, U. R., A. U. J. Lode, and B. Chatterjee, 2015, Phys. Rev. A **91**, 063621.

Foumouo, E., G. L. Kamta, G. Edah, and B. Piraux, 2006, Phys. Rev. A **74**, 063409.

Frenkel, J., 1929, *Wave Mechanics; Advanced General Theory* (Clarendon Press, Oxford).

Gajda, M., 2006, Phys. Rev. A **73**, 023603.

Girardeau, M., 1960, J. Math. Phys. (Cambridge, Mass.) **1**, 516.

Grasedyck, L., D. Kressner, and C. Tobler, 2013, GAMM Mitteilungen **36**, 53..

Greenman, L., K. B. Whaley, D. J. Haxton, and C. W. McCurdy, 2017, Phys. Rev. A **96**, 013411.

Grond, J., A. I. Streltsov, A. U. J. Lode, K. Sakmann, L. S. Cederbaum, and O. E. Alon, 2013, Phys. Rev. A **88**, 023606.

Gross, E. P., 1961, Nuovo Cimento **20**, 454.

Gwak, Y., O. V. Marchukov, and U. R. Fischer, 2018, arXiv:1811.04705.

Haldane, F. D. M., 1981, J. Phys. C **14**, 2585.

Haldar, S. K., and O. E. Alon, 2018, Chem. Phys. **509**, 72.

Haldar, S. K., and O. E. Alon, 2019, New J. Phys. **21**, 103037.

Haxton, D. J., K. V. Lawler, and C. W. McCurdy, 2011, Phys. Rev. A **83**, 063416.

Haxton, D. J., K. V. Lawler, and C. W. McCurdy, 2012, Phys. Rev. A **86**, 013406.

Haxton, D. J., K. V. Lawler, and C. W. McCurdy, 2015, Phys. Rev. A **91**, 062502.

Haxton, D. J., and C. W. McCurdy, 2014, Phys. Rev. A **90**, 053426.

Haxton, D. J., and C. W. McCurdy, 2015, Phys. Rev. A **91**, 012509.

Hochstuhl, D., and M. Bonitz, 2011, J. Chem. Phys. **134**, 084106.

Ide, Y., T. Kato, and K. Yamanouchi, 2014, Chem. Phys. Lett. **595–596**, 180.

Isinger, M., *et al.*, 2017, Science **358**, 893.

Jäckle, A., and H. D. Meyer, 1996, J. Chem. Phys. **105**, 6778.

Javanainen, J., and S. M. Yoo, 1996, Phys. Rev. Lett. **76**, 161.

Jones, J. R., *et al.*, 2016, Mol. Phys. **114**, 2014.

Jordan, G., J. Caillat, C. Ede, and A. Scrinzi, 2006, J. Phys. B **39**, S341.

Jordan, G., and A. Scrinzi, 2008, New J. Phys. **10**, 025035.

Kato, T., Y. Ide, and K. Yamanouchi, 2015, AIP Conf. Proc. **1702**, 090024.

Kato, T., and H. Kono, 2004, Chem. Phys. Lett. **392**, 533.

Kato, T., and H. Kono, 2008, J. Chem. Phys. **128**, 184102.

Kato, T., and K. Yamanouchi, 2009, J. Chem. Phys. **131**, 164118.

Kato, T., K. Yamanouchi, and H. Kono, 2018, in *Attosecond Molecular Dynamics*, Chap. 5, p. 139, https://doi.org/10.1039/9781788012669-00139.

Klaiman, S., and O. E. Alon, 2015, Phys. Rev. A **91**, 063613.

Klaiman, S., R. Beinke, L. S. Cederbaum, A. I. Streltsov, and O. E. Alon, 2018, Chem. Phys. **509**, 45.

Klaiman, S., and L. S. Cederbaum, 2016, Phys. Rev. A **94**, 063648.

Klaiman, S., A. I. Streltsov, and O. E. Alon, 2016, Phys. Rev. A **93**, 023605.

Kloss, B., I. Burghardt, and C. Lubich, 2017, J. Chem. Phys. **146**, 174107.

Koch, O., C. Neuhauser, and M. Thalhammer, 2013, ESAIM Math. Model. Numer. Anal. **47**, 1265, http://www.esaim-m2an.org/10.1051/m2an/2013067.

Köhler, F., K. Keiler, S. I. Mistakidis, H.-D. Meyer, and P. Schmelcher, 2019, J. Chem. Phys. **151**, 054108.

Kramer, P., and M. Saraceno, 2007, *Geometry of the Time-Dependent Variational Principle in Quantum Mechanics*, Lecture Notes in Physics (Springer, New York).

Krönke, S., L. Cao, O. Vendrell, and P. Schmelcher, 2013, New J. Phys. **15**, 063018.

Kvaal, S., 2011, Phys. Rev. A **84**, 022512.

Kvaal, S., 2012, J. Chem. Phys. **136**, 194109.

Kvaal, S., 2013, Mol. Phys. **111**, 1100.

Lackner, F., I. Březinová, T. Sato, K. L. Ishikawa, and J. Burgdörfer, 2015, Phys. Rev. A **91**, 023412.
Lackner, F., I. Březinová, T. Sato, K. L. Ishikawa, and J. Burgdörfer, 2017, Phys. Rev. A **95**, 033414.
Larsson, H. R., and D. J. Tannor, 2017, J. Chem. Phys. **147**, 044103.
Lee, K. S., and U. R. Fischer, 2014, Int. J. Mod. Phys. B **28**, 1550021.
Lévêque, C., and L. B. Madsen, 2017, New J. Phys. **19**, 043007.
Lévêque, C., and L. B. Madsen, 2018, J. Phys. B **51**, 155302.
Lévêque, C., and L. B. Madsen, 2019, J. Chem. Phys. **150**, 194105.
Li, X., D. J. Haxton, M. B. Gaarde, K. J. Schafer, and C. W. McCurdy, 2016, Phys. Rev. A **93**, 023401.
Li, X., C. W. McCurdy, and D. J. Haxton, 2014, Phys. Rev. A **89**, 031404.
Liao, C. T., X. Li, D. J. Haxton, T. N. Rescigno, R. R. Lucchese, C. W. McCurdy, and A. Sandhu, 2017, Phys. Rev. A **95**, 043427.
Lieb, E. H., 1963, Phys. Rev. **130**, 1616.
Lieb, E. H., and W. Liniger, 1963, Phys. Rev. **130**, 1605.
Lieb, E. H., and R. Seiringer, 2002, Phys. Rev. Lett. **88**, 170409.
Lieb, E. H., R. Seiringer, and J. Yngvason, 2000, Phys. Rev. A **61**, 043602.
Lin, R., L. Papariello, P. Molignini, R. Chitra, and A. U. J. Lode, 2019, Phys. Rev. A **100**, 013611.
Lode, A. U. J., 2016, Phys. Rev. A **93**, 063601.
Lode, A. U. J., and C. Bruder, 2016, Phys. Rev. A **94**, 013616.
Lode, A. U. J., and C. Bruder, 2017, Phys. Rev. Lett. **118**, 013603.
Lode, A. U. J., K. Sakmann, O. E. Alon, L. S. Cederbaum, and A. I. Streltsov, 2012, Phys. Rev. A **86**, 063606.
Lode, A. U. J., A. I. Streltsov, K. Sakmann, O. E. Alon, and L. S. Cederbaum, 2012, Proc. Natl. Acad. Sci. U.S.A. **109**, 13521.
Lode, A. U. J., *et al.*, 2018, New J. Phys. **20**, 055006.
Lode, A. U. J., 2015, *Tunneling Dynamics in Open Ultracold Bosonic Systems*, Springer Theses (Springer, New York), https://doi.org/10.1007/978-3-319-07085-8.
Lötstedt, E., T. Kato, and K. Yamanouchi, 2016, J. Chem. Phys. **144**, 154111.
Lötstedt, E., T. Kato, and K. Yamanouchi, 2019a, in *Springer Ser. Chem. Phys.* (Springer, Cham), Vol. 119, pp. 197–220.
Lötstedt, E., T. Kato, and K. Yamanouchi, 2019b, Phys. Rev. A **99**, 013404.
Lubich, C., and I. V. Oseledets, 2014, BIT **54**, 171.
Lubich, C., B. Vandereycken, and H. Walach, 2018, SIAM J. Numer. Anal. **56**, 1273.
Luttinger, J. M., 1963, J. Math. Phys. (N.Y.) **4**, 1154.
Madsen, L. B., C. Lévêque, J. J. Omiste, and H. Miyagi, 2018, in *Attosecond Molecular Dynamics*, Chap. 11, p. 386, https://doi.org/10.1039/9781788012669-00386.
Madsen, L. B., L. A. Nikolopoulos, T. K. Kjeldsen, and J. Fernández, 2007, Phys. Rev. A **76**, 063407.
Madsen, L. B., L. A. Nikolopoulos, and P. Lambropoulos, 2000, Eur. Phys. J. D **10**, 67.
Manthe, U., 1994, J. Chem. Phys. **101**, 2652.
Manthe, U., 2008, J. Chem. Phys. **128**, 164116.
Manthe, U., 2015, J. Chem. Phys. **142**, 244109.
Manthe, U., 2017, J. Phys. Condens. Matter **29**, 253001.
Manthe, U., H. D. Meyer, and L. S. Cederbaum, 1992, J. Chem. Phys. **97**, 3199.
Manthe, U., and T. Weike, 2017, J. Chem. Phys. **146**, 064117.
Marchukov, O. V., and U. R. Fischer, 2019, Ann. Phys. (Amsterdam) **405**, 274.
Marr, G. V., and J. B. West, 1976, At. Data Nucl. Data Tables **18**, 497.
Mattis, D. C., and E. H. Lieb, 1965, J. Math. Phys. (N.Y.) **6**, 304.
Mcguire, J. B., 1964, J. Math. Phys. (N.Y.) **5**, 622.
McLachlan, A. D., 1964, Mol. Phys. **8**, 39.
McLachlan, A. D., and M. A. Ball, 1964, Rev. Mod. Phys. **36**, 844.
Mendive-Tapia, D., T. Firmino, H. D. Meyer, and F. Gatti, 2017, Chem. Phys. **482**, 113.
Meyer, H.-D., U. Manthe, and L. S. Cederbaum, 1990, Chem. Phys. Lett. **165**, 73.
Meyer, H.-D., and H. Wang, 2018, J. Chem. Phys. **148**, 124105.
Mistakidis, S. I., G. C. Katsimiga, P. G. Kevrekidis, and P. Schmelcher, 2018, New J. Phys. **20**, 043052.
Miyagi, H., and L. B. Madsen, 2013, Phys. Rev. A **87**, 062511.
Miyagi, H., and L. B. Madsen, 2014a, J. Chem. Phys. **140**, 164309.
Miyagi, H., and L. B. Madsen, 2014b, Phys. Rev. A **89**, 063416.
Miyagi, H., and L. B. Madsen, 2017, Phys. Rev. A **95**, 023415.
Moiseyev, N., 1998, Phys. Rep. **302**, 212.
Moore, L. R., M. A. Lysaght, J. S. Parker, H. W. Van Der Hart, and K. T. Taylor, 2011, Phys. Rev. A **84**, 061404.
Mueller, E. J., T.-L. Ho, M. Ueda, and G. Baym, 2006, Phys. Rev. A **74**, 033612.
Nest, M., 2009, Chem. Phys. Lett. **472**, 171.
Nest, M., R. Padmanaban, and P. Saalfrank, 2007, J. Chem. Phys. **126**, 214106.
Nest, M., F. Remacle, and R. D. Levine, 2008, New J. Phys. **10**, 025019.
Nguyen, J. H., M. C. Tsatsos, D. Luo, A. U. J. Lode, G. D. Telles, V. S. Bagnato, and R. G. Hulet, 2019, Phys. Rev. X **9**, 011052.
Nozieres, P., and D. St. James, 1982, J. Phys. (Paris) **43**, 1133.
Ohmura, S., T. Kato, T. Oyamada, S. Koseki, H. Ohmura, and H. Kono, 2018, J. Phys. B **51**, 034001.
Ohmura, S., H. Kono, T. Oyamada, T. Kato, K. Nakai, and S. Koseki, 2014, J. Chem. Phys. **141**, 114105.
Olsen, J., B. O. Roos, P. Jørgensen, and H. J. A. Jensen, 1988, J. Chem. Phys. **89**, 2185.
Omiste, J. J., W. Li, and L. B. Madsen, 2017, Phys. Rev. A **95**, 053422.
Omiste, J. J., and L. B. Madsen, 2018, Phys. Rev. A **97**, 013422.
Omiste, J. J., and L. B. Madsen, 2019, J. Chem. Phys. **150**, 084305.
Orimo, Y., T. Sato, and K. L. Ishikawa, 2019, Phys. Rev. A **100**, 013419.
Orimo, Y., T. Sato, A. Scrinzi, and K. L. Ishikawa, 2018, Phys. Rev. A **97**, 023423.
Pazourek, R., S. Nagele, and J. Burgdörfer, 2015, Rev. Mod. Phys. **87**, 765.
Pedersen, T. B., and S. Kvaal, 2019, J. Chem. Phys. **150**, 144106.
Penrose, O., and L. Onsager, 1956, Phys. Rev. **104**, 576.
Pitaevskii, L. P., 1961, Sov. Phys. JETP **13**, 451, http://www.jetp.ac.ru/cgi-bin/e/index/e/13/2/p451?a=list.
Raab, A., and H. D. Meyer, 2000, Theor. Chem. Acc. **104**, 358.
Rescigno, T. N., and A. E. Orel, 1991, Phys. Rev. A **43**, 1625.
Rook, T., 2006, *Essentials of Computational Chemistry Theories and Models* (Wiley, New York), Vol. 73.
Roy, R., C. Lévêque, A. U. J. Lode, A. Gammal, and B. Chakrabarti, 2019, Quantum Reports **1**, 304.
Röpke, G., 1999, *Quantum Mechanics, Special Chapters* (Springer, New York), Vol. 213.
Sakmann, K., 2011, *Many-Body Schrödinger Dynamics of Bose-Einstein Condensates*, Springer Theses (Springer, New York).
Sakmann, K., and M. Kasevich, 2016, Nat. Phys. **12**, 451.
Sakmann, K., and J. Schmiedmayer, 2018, arXiv:1802.03746.
Sakmann, K., A. I. Streltsov, O. E. Alon, and L. S. Cederbaum, 2008, Phys. Rev. A **78**, 023615.
Sakmann, K., A. I. Streltsov, O. E. Alon, and L. S. Cederbaum, 2009, Phys. Rev. Lett. **103**, 220601.

Sakmann, K., A. I. Streltsov, O. E. Alon, and L. S. Cederbaum, 2010, Phys. Rev. A **82**, 013620.
Sakmann, K., A. I. Streltsov, O. E. Alon, and L. S. Cederbaum, 2011, New J. Phys. **13**, 043003.
Sakmann, K., A. I. Streltsov, O. E. Alon, and L. S. Cederbaum, 2014, Phys. Rev. A **89**, 023602.
Samson, J. A., and W. C. Stolte, 2002, J. Electron Spectrosc. Relat. Phenom. **123**, 265.
Sato, T., and K. L. Ishikawa, 2013, Phys. Rev. A **88**, 023402.
Sato, T., and K. L. Ishikawa, 2015, Phys. Rev. A **91**, 023417.
Sato, T., H. Pathak, Y. Orimo, and K. L. Ishikawa, 2018a, J. Chem. Phys. **148**, 051101.
Sato, T., H. Pathak, Y. Orimo, and K. L. Ishikawa, 2018b, in *Opt. InfoBase Conf. Pap.* (Optical Society of America), Volume Part F125-, p. 21a_221B_4, arXiv:1712.09044.
Sawada, R., T. Sato, and K. L. Ishikawa, 2016, Phys. Rev. A **93**, 023434.
Schneider, B. I., and T. N. Rescigno, 1988, Phys. Rev. A **37**, 3749.
Schollwöck, U., 2005, Rev. Mod. Phys. **77**, 259.
Schollwöck, U., 2011, Ann. Phys. (N.Y.) **326**, 96.
Schultze, M., *et al.*, 2010, Science **328**, 1658.
Selstø, S., and S. Kvaal, 2010, J. Phys. B **43**, 065004.
Sherrill, C. D., and H. F. Schaefer, 1999, Adv. Quantum Chem. **34**, 143.
Siegl, P., S. I. Mistakidis, and P. Schmelcher, 2018, Phys. Rev. A **97**, 053626.
Spekkens, R. W., and J. E. Sipe, 1999, Phys. Rev. A **59**, 3868.
Streltsov, A. I., 2013, Phys. Rev. A **88**, 041602.
Streltsov, A. I., O. E. Alon, and L. S. Cederbaum, 2006, Phys. Rev. A **73**, 063626.
Streltsov, A. I., O. E. Alon, and L. S. Cederbaum, 2007, Phys. Rev. Lett. **99**, 030402.
Streltsov, A. I., O. E. Alon, and L. S. Cederbaum, 2008, Phys. Rev. Lett. **100**, 130401.
Streltsov, A. I., O. E. Alon, and L. S. Cederbaum, 2009, Phys. Rev. A **80**, 043616.
Streltsov, A. I., O. E. Alon, and L. S. Cederbaum, 2011, Phys. Rev. Lett. **106**, 240401.
Streltsova, O. I., O. E. Alon, L. S. Cederbaum, and A. I. Streltsov, 2014, Phys. Rev. A **89**, 061602.
Sukiasyan, S., C. McDonald, C. Destefani, M. Y. Ivanov, and T. Brabec, 2009, Phys. Rev. Lett. **102**, 223002.
Sukiasyan, S., S. Patchkovskii, O. Smirnova, T. Brabec, and M. Y. Ivanov, 2010, Phys. Rev. A **82**, 043414.
Sutherland, B., 1971, J. Math. Phys. (N.Y.) **12**, 251.
Swann, W. F., 1929, J. Franklin Inst. **207**, 457.
Szabo, A., and N. L. Ostlund, 1996, *Modern Quantum Chemistry: Introduction to Advanced Electronic Structure Theory* (Dover Publications, New York).
Tao, L., and A. Scrinzi, 2012, New J. Phys. **14**, 013021.
Theisen, M., and A. I. Streltsov, 2016, Phys. Rev. A **94**, 053622.
Tsatsos, M. C., and A. U. J. Lode, 2015, J. Low Temp. Phys. **181**, 171.
Ulusoy, I. S., and M. Nest, 2012, J. Chem. Phys. **136**, 054112.
Vendrell, O., and H. D. Meyer, 2011, J. Chem. Phys. **134**, 044135.
Wang, H., 2015, J. Phys. Chem. A **119**, 7951.
Wang, H., and M. Thoss, 2003, J. Chem. Phys. **119**, 1289.
Wang, H., and M. Thoss, 2009, J. Chem. Phys. **131**, 024114.
Wang, H., and M. Thoss, 2016, J. Chem. Phys. **145**, 164105.
Wang, H., and M. Thoss, 2018, Chem. Phys. **509**, 13.
Weike, T., and U. Manthe, 2020, J. Chem. Phys. **152**, 034101.
Weiner, S. E., M. C. Tsatsos, L. S. Cederbaum, and A. U. J. Lode, 2017, Science Reports **7**, 40122.
Wodraszka, R., and T. Carrington, 2017, J. Chem. Phys. **146**, 194105.
Worth, G., H.-D. Meyer, and L. Cederbaum, 1999, Chem. Phys. Lett. **299**, 451.
Worth, G. A., H.-D. Meyer, and L. S. Cederbaum, 1998, J. Chem. Phys. **109**, 3518.
Yan, J., 2003, J. Stat. Phys. **113**, 623.
Yukalov, V. I., and M. D. Girardeau, 2005, Laser Phys. Lett. **2**, 375.
Yukalov, V. I., A. N. Novikov, and V. S. Bagnato, 2014, Laser Phys. Lett. **11**, 095501.
Yukalov, V. I., A. N. Novikov, and V. S. Bagnato, 2015, Phys. Lett. A **379**, 1366.
Załuska-Kotur, M. A., M. Gajda, A. Orłowski, and J. Mostowski, 2000, Phys. Rev. A **61**, 033613.
Zanghellini, J., M. Kitzler, T. Brabec, and A. Scrinzi, 2004, J. Phys. B **37**, 763.
Zanghellini, J., M. Kitzler, C. Fabian, T. Brabec, and A. Scrinzi, 2003, Laser Phys. **13**, 1064.
Zwolak, M., and G. Vidal, 2004, Phys. Rev. Lett. **93**, 207205.